Atmos. Chem. Phys. Discuss., doi:10.5194/acp-2015-970, 2016
Manuscript under review for journal Atmos. Chem. Phys.
Published: 19 January 2016

Atmospheric Chemistry and Physics Discussions

Controls on phase composition and ice water content in a convection permitting model simulation of a tropical mesoscale convective system

C.N. Franklin[1], A. Protat[2], D. Leroy[3] and E. Fontaine[3]

[1]{CSIRO, Oceans and Atmosphere, Aspendale, Victoria, Australia}

[2]{Bureau of Meteorology, Docklands, Victoria, Australia}

[3]{Laboratoire de Meteorologie Physique, Universite Blaise Pascal, Clermont-Ferrand, France}

Correspondence to: C. N. Franklin (charmaine.franklin@csiro.au)

Abstract

Simulations of tropical convection from an operational numerical weather prediction model are evaluated with the focus on the model's ability to simulate the observed high ice water contents associated with the outflow of deep convection and to investigate the modelled processes that control the phase composition of tropical convective clouds. The intensification and decay of convective strength across the mesoscale convective system lifecycle is simulated well, however, the areas with reflectivities > 30 dBZ are overestimated due to too much rain above the freezing level, stronger updrafts and larger particle sizes in the model. The inclusion of a heterogeneous rain freezing parameterisation and the use of different ice size distributions show better agreement with the observed reflectivity distributions, however, this simulation still produces a broader profile with many high reflectivity outliers demonstrating the greater occurrence of convective cells in the simulations. It is shown that the growth of ice is less dependent on vertical velocity than is liquid water, with the control on liquid water content being the updraft strength due to stronger updrafts having minimal entrainment and higher supersaturations. Larger liquid water contents are produced when cloud droplet number concentrations are increased or when a parameterisation of heterogeneous freezing of rain is included. These changes reduce the efficiency of the warm rain processes in the model generating greater supercooled liquid water contents. The control

Atmos. Chem. Phys. Discuss., doi:10.5194/acp-2015-970, 2016
Manuscript under review for journal Atmos. Chem. Phys.
Published: 19 January 2016

Atmospheric Chemistry and Physics Discussions

on ice water content in the model is the ice sizes and available liquid water, with the larger ice particles growing more efficiently via accretion and riming. Limiting or excluding graupel produces larger ice water contents for warmer temperatures due to the greater ice mass contained in slow falling snow particles. This results in longer in-cloud residence times and more efficient removal of liquid water. It is demonstrated that entrainment in the mixed-phase regions of convective updrafts is most sensitive to the turbulence formulation in the model. Greater mixing of environmental air into cloudy updrafts in the region of -30 to 0 degrees Celsius produces more detrainment at these temperatures and the generation of a larger stratiform area. Above these levels in the purely ice region of the updrafts, the entrainment and buoyancy of air parcels is controlled by the ice particle sizes, demonstrating the importance of the microphysical processes on the convective dynamics.

1 Introduction

Improving the simulation of tropical convective clouds in convection-permitting simulations is an important yet challenging endeavour. Forecasting centres are beginning to use operational numerical weather prediction models with horizontal grid spacing of order 1 km and while these models have been shown to improve the diurnal cycle of convection and the distribution of rain rates (e.g. Clark et a. 2007; Weusthoff et al. 2010), there are numerous deficiencies at these resolutions that impacts the accuracy of the forecasts and the confidence in using these models to help guide parameterisation development for coarser resolution models and develop retrieval algorithms for remotely sensed cloud properties (e.g. Del Genio and Wu 2010; Shige et al. 2009). One salient aspect of forecasting tropical meteorology is the high ice water contents that are responsible for numerous aircraft safety incidents as discussed by Fridlind et al. (2015). These incidents tend to occur in fully glaciated conditions in the vicinity of deep convection where high ice water contents can cause engine power loss (e.g. Lawson et al. 1998; Mason et al. 2006; Strapp et al. 2015). In recognition of this an international field campaign called the High Ice Water Content (HIWC) study was conducted out of Darwin in the beginning of 2014 and provided a high quality database of ice cloud measurements associated with deep tropical convective systems. These observations are a valuable resource for evaluating convection permitting model simulations and cloud microphysical parameterisations. In this work cloud properties are evaluated from an operational model with the focus on the model's ability to simulate high ice water contents

generated from the outflow of deep convection and to understand what modelled processes control the phase composition of the simulated tropical convective clouds.

Many previous convection permitting simulations of tropical convection have documented common biases amongst models including excessive reflectivities above the freezing level, lack of stratiform cloud and precipitation and too much frozen condensate (e.g. Blossey et al. 2007; Lang et al. 2011; Fridlind et al. 2012; Varble et al. 2014a,b). Lang et al. (2011) modified a single moment microphysics scheme to reduce the biases in simulated radar reflectivities and ice sizes in convective systems and found better success in a weakly organised continental convective case compared to a stronger oceanic MCS. The reason could be due to dynamical errors in the model that had a greater influence on the microphysical characteristics in the simulations of stronger convection. Varble et al. (2014a) compared cloud resolving and limited area model simulations with the extensive database of observations from the Tropical Warm Pool-International Cloud Experiment. They found excessive vertical velocities even at 100 m horizontal grid spacings and suggested that the overly intense updrafts are a product of interactions between the convective dynamics and microphysics. These strong updrafts transport condensate and moisture to the upper levels that contributes to the larger amount of frozen condensate seen in simulations, and the reduced detrainment at lower levels could play a role in the lack of generation of significant stratiform cloud and precipitation (Ferrier 1994; Tao et al. 1995; Morrison et al. 2009). In the operational model used in this study the microphysics scheme is a single moment bulk scheme. Model intercomparison studies have shown that double moment microphysics schemes do not necessarily perform better than single moment schemes, and in fact provided that the intercept parameters are not fixed and are able to vary, these more simple schemes can match or even outperform the more complex double moment schemes in their representation of cloud and rainfall properties (e.g. VanWeverberg et al. 2013; Varble et al. 2014b).

The aims of this study are twofold: firstly to test different configurations of the dynamics, turbulence and microphysical formulations in the model to determine those that best represent tropical convective cloud systems and to understand the sensitivities in the modelled cloud and dynamical properties to these changes, and; secondly to determine what process control the phase composition and ice water content in the model. The following section describes the model and observations used in this work. Section 3 compares the simulations with the available observations including: a time series comparison with the satellite data, comparison

Atmos. Chem. Phys. Discuss., doi:10.5194/acp-2015-970, 2016
Manuscript under review for journal Atmos. Chem. Phys.
Published: 19 January 2016

Atmospheric Chemistry and Physics Discussions

of the simulated radar reflectivity characteristics with those from the Darwin radar and an investigation into the controls on phase composition in the model and how the IWC and ice particle sizes compare with the in situ observations. This is followed by a summary of the results in section 4.

2 Description of the model and observations

The Met Office Unified Model (UM) version 8.5 is used to create a series of one-way nested simulations. The global model configuration GA6 (Walters et al. 2015) is the driving model, which uses the Even Newer Dynamics for General atmospheric modelling of the environment (ENDGame) dynamical core (Wood et al. 2014). The global model has a resolution of N512 (~ 25 km) with 70 vertical levels and is run with a 10 minute time step. The convection scheme is based on Gregory and Rowntree (1990) and uses a vertical velocity dependent convective available potential energy (CAPE) closure. The Prognostic Cloud Prognostic Condensate (PC2) scheme of Wilson et al. (2008) is used with the microphysics scheme described by Wilson and Ballard (1999) but with numerous modifications including prognostic rain and graupel, cloud droplet settling and the Abel and Boutle (2012) rain drop size distribution. The boundary layer scheme used is based on Lock et al. (2000) and the radiative fluxes are determined by the Edwards and Slingo (1996) scheme. The global model is initialised at 00 UTC using the Australian Community Climate and Earth System Simulator (ACCESS; Puri et al. 2013) operational analysis for the case study date of February 18 2014.

The first nested simulation within the global model is a 4 km grid length simulation. These simulations are run with a 100 s time step and are forced at the boundaries every 30 minutes. At this resolution the Smith (1990) diagnostic cloud scheme is used where the critical relative humidity is 0.8 above 800 m and increases to 0.96 at the lowest model level. The cloud microphysical parameterisations are the same as the global model except that the generic ice particle size distribution (PSD) scheme of Field et al. (2007) is used. The convection scheme at this resolution has a modified CAPE closure that scales with grid-box area, which allows for more of the convective activity to be modelled explicitly. The other difference from the global model is the diffusion. While there is no horizontal diffusion in the global model, in the 4 km model this is modelled by a Smagorinsky (1963) type scheme and the vertical diffusion coefficients are determined using a scheme that blends those from the boundary layer scheme and the Smagorinsky scheme (Boutle et al. 2014). The older dynamics scheme (named New Dynamics; Davies et al. 2005) is used in the control model configuration as that dynamical

Atmos. Chem. Phys. Discuss., doi:10.5194/acp-2015-970, 2016
Manuscript under review for journal Atmos. Chem. Phys.
Published: 19 January 2016

Atmospheric Chemistry and Physics Discussions

core was the one being used in the high resolution operational model forecasts for this version of the model. However, the effects of the dynamics are also tested by using ENDGame in a sensitivity experiment.

A suite of 1 km simulations are nested in the 4 km simulation that investigates the effects of the dynamics, turbulence and microphysical parameterisations on the simulations of tropical convective clouds. There are 80 vertical levels and the model is run with a time step of 30 s. The domain is 500 x 500 km^2 centred on the location of the Darwin radar (12.25 °S, 131.04 °E) as shown in Figure 1 and the convection is modelled explicitly. Given that the focus of this work is primarily on the cloud microphysics, a description of the scheme used in the model is provided, with the details of the other parameterisations available in the previously cited references. The microphysics scheme is described by Wilson and Ballard (1999) but with numerous modifications. The single moment scheme carries water in four variables: vapour, liquid, ice and rain, with an additional graupel variable in the 1 and 4 km simulations. The 4 km and control version of the 1 km model use the generic ice particle size distribution of Field et al. (2007), where the aggregates and crystals are represented by a single prognostic aggregate variable. This parameterisation is based on the idea of relating moments of the size distribution to the second moment, which is directly proportional to the ice water content when mass is equal to the square of the particle size. In using this parameterisation there is no need to specify an intercept parameter for the PSD and instead the microphysical transfer rates are derived from the moment estimation parameterisation that is a function of ice water content and temperature. The mass-diameter relationships take the form of a power law

$$m(D) = aD^b \quad (1)$$

The particle size distributions are generalised gamma functions

$$N(D) = N_0 D^{\mu} e^{-\lambda D} \quad (2)$$

where N_0 is the intercept parameter, μ is the shape parameter and λ is the slope parameter. The coefficients for each hydrometeor species are given in Table 1, where the aggregate and crystal PSD coefficients are for the simulations that use an explicit PSD and not the generic ice PSD parameterisation. The explicit ice size distributions have a temperature-dependent intercept parameter that decreases with warming temperatures, representing larger particles and the effect of aggregation (Houze et al. 1979), where in Table 1

Atmos. Chem. Phys. Discuss., doi:10.5194/acp-2015-970, 2016
Manuscript under review for journal Atmos. Chem. Phys.
Published: 19 January 2016

Atmospheric Chemistry and Physics Discussions

$$f(T) = \exp\left(-\frac{\max(Tc, -45°C)}{8.18°C}\right) \quad (3)$$

following Cox (1988) with T_c the temperature in degrees Celsius. Fall speeds are parameterised from power laws with the coefficients for crystals and aggregates from Mitchell (1996), graupel from Ferrier (1994) and rain from Abel and Shipway (2007).

Ice can be formed by homogeneous and heterogeneous nucleation processes. At -40 °C and below, homogeneous nucleation instantaneously converts all liquid water (both cloud water and rain) to ice. Heterogeneous nucleation requires cloud water to be present at temperatures at or below -10 °C. The process is dependent on relative humidity and the mass of the number of active nuclei produced from the temperature dependent function from Fletcher (1962). Once ice has been formed it can grow by vapour deposition, riming, collection and aggregation. The autoconversion of snow to graupel occurs when snow growth is dominated by riming, with the additional conditions that the snow mass threshold is exceeded and the temperature is below -4 °C. Once graupel has formed it grows by riming and collection. The ice hydrometeors experience sublimation, evaporation and melting. There are a number of graupel transfer terms that have not been included in the model as their rates are significantly smaller than the dominant processes (Wilkinson et al. 2013). The graupel terms not included are: deposition and sublimation; wet mode growth; collection of ice crystals; and freezing rain.

The control model (denoted as nd) in the set of 1km simulations uses the New Dynamics and the sensitivity to dynamical formulation is investigated by testing the ENDGame dynamical core in the simulation denoted eg. Modelling the vertical turbulent mixing using the 3D Smagorinsky scheme rather than the blended scheme used in the control simulation is labelled 3d. The other experiments test aspects of the microphysical parameterisations:

nopsd – Rather than use the generic ice PSD as in the control experiment, explicit PSDs are used for ice where the single ice prognostic is diagnostically split as a function of the temperature difference from cloud top into two categories to represent the smaller more numerous ice crystals and larger aggregates (Wilkinson et al. 2013).

qcf2 – As for nopsd but the crystals and aggregates are represented as two separate prognostic variables.

Atmos. Chem. Phys. Discuss., doi:10.5194/acp-2015-970, 2016
Manuscript under review for journal Atmos. Chem. Phys.
Published: 19 January 2016

qcf2hm – As for qcf2 but with the inclusion of an ice splintering parameterisation that increases the deposition rate in the Hallett-Mosssop (1974) temperature zone of -3 to -8 °C. This parameterisation represents the increase in the ice particle number concentration due to ice splinter production during riming and is dependent on the supercooled liquid water content, and as such the riming rate, as well as the temperature that allows for increased deposition at temperatures colder than -8 °C due to the vertical transport of ice splinters (Cardwell et al. 2002).

qcf2ndrop500 – As for qcf2 but with an increase in the cloud droplet number concentration from 100 cm^{-3} to 500 cm^{-3}.

qcf2sr2graupel – As for qcf2 but with the restriction that snow-rain collisions do not produce graupel.

qcf2noqgr – As for qcf2 but without the inclusion of graupel.

qcf2rainfreeze – As for qcf2 but with the inclusion of a heterogeneous rain freezing parameterisation based on the stochastic parameterisation of Bigg (1953) following Wisner et al. (1972).

qcf2raindsd – As for qcf2 but with the Marshall-Palmer (1948) rain drop size distribution.

The Darwin C-band polarimetric (CPOL) radar (Keenan et al. 1998) collects a 3D volume of observations out to a range of 150 km. The radar observations have been interpolated onto the model 1 km grid, and the analysis of radar reflectivities is for the area encompassed by the radius < 150 km from the radar (see Fig. 1). The precipitation rates derived from the radar reflectivity have uncertainties of 25% at rain rates greater than 10 mm hr^{-1} and 100% for the lowest rain rates (Fridlind et al. 2012). The satellite observations of outgoing longwave radiation (OLR), cloud top height and ice water path (IWP) were derived from the geostationary satellite MTSAT-1R following Minnis and Smith (1998) and Minnis et al. (2008; 2011). Observations from the French Falcon 20 aircraft are from research flight 23. The ice water content (IWC) measurement was made with the isokinetic evaporator probe IKP-2 (Davison et al. 2009), and the ice sizes are from the 2D-Stereo (Lawson et al. 2006) and precipitation imaging probes (Baumgardner et al. 2001). Processing of the size observations accounted for possible ice shattering by consideration of the inter-arrival times and the ratio between the particle surface and lengths (Leroy et al. 2015).

Atmos. Chem. Phys. Discuss., doi:10.5194/acp-2015-970, 2016
Manuscript under review for journal Atmos. Chem. Phys.
Published: 19 January 2016

Atmospheric Chemistry and Physics Discussions

3 Comparison of the simulations with observations

On February 18 2014 the monsoon trough was stalled near the base of the Top End with active conditions continuing about the northern coast. There was a deep moisture layer and low level convergence that produced a mesoscale convective system. At 12 UTC satellite imagery shows the convection around Darwin was somewhat isolated in nature, with a convective cell developing close to the radar by 15 UTC (not shown). This convection developed into a larger organised mesoscale convective system by 18 UTC with deep convective cells producing cloud top temperatures of -80 °C. A widespread region of anvil cloud produced from the outflow of deep convection was seen to develop from 18 UTC and persist for over 8 hours. The HIWC research flight penetrated convective cores in a region northeast of the radar at 22 – 24 UTC (Fig. 1) with peak ice water content up to 5 g m^{-3}.

The sounding at 23 UTC (Figure 2) shows a temperature of 24 °C at 70 m and an unstable environmental lapse rate, with the temperature gradient reducing at 700 hPa. This height corresponds to the typical cloud base in the region as observed by satellite at about 3 km and saturation is observed at the freezing level at 4.6 km (570 hPa). The control 1 km model shows a reasonable representation of the low level temperature up to 800 hPa, where the model is then warmer up to 600 hPa. This simulation is drier in the levels below 4 km and then has excessive moisture throughout the mid and upper troposphere, maintaining saturated air with a warm bias present from 400 hPa (7 km). The upper level moisture bias is not present in the global model simulation, however it is apparent in the 4 km simulation. This bias is seen in the relative humidity regardless of whether the individual model grid box at the sounding location is used as in Figure 1 or whether an area averaged domain is used as shown in Figure 4a. At this time the model simulates almost completely overcast conditions, which compares well to the satellite observed cloud cover of 95%. Excessive moisture in small domain simulations is a common error related to the limited domain size that does not allow for sufficient mesoscale organisation of convection and humidity (Bretherton et al. 2005). Given that the 4 km simulation also shows this error and the domain size in that case is 2000 x 2000 km^2, it seems that the upper tropospheric moisture errors in this case are not predominately driven by the domain size.

The observed winds tend to be from the south-east in the lowest few kilometres and turn clockwise to persist as westerlies from 6 – 12 km. Above this height the wind shifts to be from the east with the largest wind speeds occurring above 14 – 15 km > 20 m s^{-1} (note this is

Atmos. Chem. Phys. Discuss., doi:10.5194/acp-2015-970, 2016
Manuscript under review for journal Atmos. Chem. Phys.
Published: 19 January 2016

above the pressure range shown in Figure 2). These wind profiles tend to be associated with the active monsoon at Darwin where the migration of the monsoon trough reverses the large-scale circulation (Fein and Stephens 1987). The height of the largest vertical wind shear in the simulations is a couple of kilometres too high but the magnitude and direction of the strong upper level easterlies is represented well. The winds are too strong in the simulations between 1.5 and 4 km and do not have the same easterly component, however, above this level the wind speed is reasonably captured, with these deep westerly winds providing the source of moisture for the deep convective clouds observed and simulated.

3.1 Time series comparison with observations

The domain mean precipitation rates and ice water path (IWP) shown in Figure 3 demonstrate that a larger IWP implies a larger surface rainfall rate as seen in previous tropical studies (e.g. Liu and Curry 1999). The radar derived precipitation shows that the simulations overestimate the domain mean rainfall rate during the development stages of the MCS, and produce the peak in precipitation about 2 hours earlier than is observed. The model precipitation maximum occurs when the simulated convection is strongest, as measured by the largest domain mean vertical velocity at 500 hPa and the maximum vertical velocities. The observed domain mean rainfall maximum corresponds to the time when the domain mean cloud top height is highest, and together with the observed brightness temperatures (not shown), suggests that the generation of significant anvil cloud occurs before the domain mean precipitation maximum, rather than when the convection is strongest as is the case in the simulations. Note that the simulated domain mean precipitation rate at both the earlier and later times is outside of the uncertainty range of the radar derived rainfall rate (Fridlind et al. 2012).

The underestimate in surface rainfall for the later times when the MCS has matured is not due to an underestimate in the domain mean upper tropospheric cloud cover as both the model and satellite observations show mostly overcast conditions, but rather the underestimate in condensate reaching below the freezing level (as will be demonstrated in the following subsection), which is partly due to a drier lower troposphere as shown in Figures 2 and 4. The observed IWP is only valid for the daytime from about 22:30 UTC or 8 am local time, and while the simulations with the generic PSD parameterisation compare well with the satellite derived value, the comparison of VISST IWP with CloudSat in tropical regions was shown by Waliser et al. (2009) to be underestimated by 25%, likely due to the maximum retrieved

Atmos. Chem. Phys. Discuss., doi:10.5194/acp-2015-970, 2016
Manuscript under review for journal Atmos. Chem. Phys.
Published: 19 January 2016

Atmospheric Chemistry and Physics Discussions

optical depth being limited to 128. This suggests that the modelled domain mean IWP may be underestimated from 22:30 – 23:30 UTC. Other studies have documented the lack of stratiform rainfall in convective-scale simulations and some attributed the error to excessive evaporation in single-moment microphysics schemes that use a constant intercept parameter in the rain DSD (Morrison et al. 2009). That is not the case in this work and rather the cause is likely due to overly strong convection (Sect 3.2.3) that detrains too high and does not produce enough condensate in the lower stratiform regions as has been shown by Ferrier (1994), Tao et al. (1995) and Morrison et al. (2009).

The greater IWP in the simulations that use the generic ice PSD parameterisation is associated with larger relative humidity in the upper troposphere (Figure 4a). In a study comparing different microphysics schemes, VanWeverberg et al. (2013) found the same result and associated the increased moisture with the sublimation of ice particles due to the scheme with the slowest ice fall speeds producing the greatest condensate and moisture. That is not the case for this current study where the larger IWP and relative humidity is produced by the microphysics configuration that produces larger particle sizes (Figure 4c) but similar ice fall speeds above about 12 km, with faster below this height. Figure 4b shows the fall speeds for the ice crystals and aggregates/snow particles. All simulations use the same formulation for snow and even though the generic PSD only represents a single hydrometeor category there are two fall speeds used to enable a representation of both fast and slow sedimenting particles based on size. The method when using the generic PSD is described by Furtardo et al. (2014) where for narrow size distributions and small mean sizes the fall speed used is that shown for the ice crystals in Figure 4b, and for broader size distributions and larger mean sizes the snow fall speed is used (the cross over is around 600 µm). Looking at the mean ice particles sizes in Figures 4c and 4d shows larger sizes for the simulations that use the generic PSD, however, the slower ice crystal fall speed used in these cases produces a similar mean fall speed to the simulations that use two ice prognostics. The higher RH in the simulations using the generic ice PSD is due to the larger, faster falling particles in the levels below 12 km removing more of the LWC via riming (explored later in Section 3.3), which allows for greater supersaturation. More riming releases more latent heat, which along with the larger ice particles being more effectively off-loaded, generates stronger updrafts with less entrainment and higher RH in the upper troposphere. This is illustrated in the horizontal mass divergence profiles shown in Figure 5. As discussed by Yuter and Houze (1995) the presence of decelerating updrafts and accelerating downdrafts can be largely explained by entrainment.

Atmos. Chem. Phys. Discuss., doi:10.5194/acp-2015-970, 2016
Manuscript under review for journal Atmos. Chem. Phys.
Published: 19 January 2016

Entrainment reduces the buoyancy of updrafts, slowing and eventually stopping the air parcel, which is where divergence is expected. In contrast, entrainment into downdrafts enhances evaporative cooling, increasing the downward mass transport and convergence. The simulations that use the generic ice PSD produce less horizontal mass divergence in the levels above 12 km, suggesting reduced entrainment and deposition of mass at these heights. Instead updrafts in these simulations tend to penetrate higher, in agreement with Figure 3. Figure 5 shows that entrainment in the mixed-phase regions of the convective updrafts is the most sensitive to the turbulence formulation in the model, with the simulation with greater turbulent mixing (3d) showing greater mass divergence and entrainment in the range of 5 – 7 km. This contrasts to the upper ice only regions of the updrafts that show that the largest control on entrainment and buoyancy is the ice sizes. The simulations with smaller sized particles have more horizontal mass divergence above 12 km, indicating a larger reduction in the buoyancy in the upper levels than the simulations with larger sized ice particles.

The satellite retrieved cloud top height shows a variation in domain mean of greater than 2 km over the 12 hours of the MCS lifecycle analysed (Fig. 3c). The simulations show typically only a 500 metre change, reducing from 12 – 24 UTC. While the domain mean cloud top height agrees reasonably well with the satellite observations, the outgoing longwave radiation (OLR) does not with the simulations reducing the OLR by 50 – 100 W m^{-2} too much (Fig. 3d). The simulations that use the generic ice PSD have higher cloud tops with colder temperatures and greater IWP that produce lower OLR than the simulations that use explicit ice PSDs (20 – 30 W m^{-2} lower) and the observations (~80 W m^{-2} lower). The minimum observed OLR at 20 UTC is captured by most of the simulations, with the simulations then tending to increase OLR at a faster rate than is observed as the MCS structure matures to be composed of mostly stratiform cloud.

3.2 Radar reflectivity characteristics

The model hydrometeor fields have been converted into radar reflectivities by assuming Rayleigh scattering, with no consideration of the effects of attenuation or attempt to model the radar bright band. Due to the long wavelength of the CPOL radar (5.3 cm) modelled reflectivity is calculated following Hogan et al. (2006) where the reflectivity is considered proportional to mass squared

Atmos. Chem. Phys. Discuss., doi:10.5194/acp-2015-970, 2016
Manuscript under review for journal Atmos. Chem. Phys.
Published: 19 January 2016

Atmospheric Chemistry and Physics Discussions

$$Z = R\int_0^\infty M(D)^2 N(D) dD \quad (4)$$

where $R = 10^{18}\frac{|K|^2}{0.93}\left(\frac{6}{\pi\rho}\right)^2$, ρ is the particle density and the mass M and particle size distribution $N(D)$ are defined by (1) and (2). For cloud liquid water the reflectivity is calculated from the constant number concentration of 100 cm^{-3} in the simulations with the size distribution $N(D) = PD^2 \exp^{-\lambda D}$, where $P = N/2\lambda^3$ following McBeath et al. (2014). The dielectric factor $|K|^2$ is set to 0.93 for water and 0.174 for ice. The particle densities used in the calculation of R are 1000 kg m^{-3} for rain, 917 kg m^{-3} for aggregates and crystals and 500 kg m^{-3} for graupel. For the simulations that use the generic ice PSD parameterisation, the aggregate reflectivity is proportional to the 4th moment of the PSD, which is calculated from the Field et al. (2007) moment estimation parameterisation.

3.2.1 Statistical radar coverage analysis

To examine the temporal evolution of the mesoscale convective system and evaluate the modelled MCS lifecycle and the simulated reflectivities, a statistical coverage product has been produced following May and Lane (2009). The data used to construct the statistical product are reflectivity fields from CPOL and the simulations every 30 minutes for 12 hours from 12 – 24 UTC. At each height the fraction of the total area within the radar domain covered by reflectivity thresholds is calculated, with the thresholds chosen as 10, 20, 30 and 40 dBZ.

The observed statistical radar coverage product shown in Figure 6 illustrates the development of the MCS. At 12 UTC the radar domain has a low fractional area coverage of up to 0.15 for the 10 dBZ threshold, showing that at 12 UTC there were hydrometeors covering 5 – 15% of the radar sampling area between the lowest detectable altitude of 1.5 km and 8 km. Highest cloud tops of 11 km are seen in the > 10 dBZ fractional coverage at 17:30 UTC, which coincides with the time that the very cold cloud tops associated with deep convective cells were seen in the satellite imagery. The maximum coverage of the domain by hydrometeors with reflectivities > 10 dBZ is 85% seen at 21 – 22 UTC, which is when the large anvil cloud shield appears a few hours after the deepest convection occurs. The observed areas of reflectivity > 10 dBZ are fairly uniform with height from 2 – 6 km demonstrating little variability of the hydrometeor coverage from the low levels to a couple of km above the

Atmos. Chem. Phys. Discuss., doi:10.5194/acp-2015-970, 2016
Manuscript under review for journal Atmos. Chem. Phys.
Published: 19 January 2016

freezing level. Fractional areas larger than 0.05 with reflectivities > 20 dBZ are mostly confined to below 6 km, with the maximum fraction of 0.65 occurring at 21 UTC at 4 km. The > 30 dBZ area is not greater than 10% until 16 UTC, and is maximum between 20:30 – 22 UTC at 4 km with a value of 0.35. There is no fractional area of the domain > 0.05 that contains observed reflectivities greater than 40 dBZ.

While the statistical radar coverage product produced for the control simulation does show a transition from scattered to more organised convection with widespread stratiform cloud regions and predicts the timing of the deepest clouds generally well (Fig. 6), there are clear deficiencies in the simulated evolution of the MCS. There are much larger high dBZ fractional areas, deeper clouds occur too early in the simulation and there is a strong vertical gradient in the area coverage with height. The less uniform vertical area coverage shows that the simulated clouds have more variability in reflectivity with height compared to the observations. In coarse resolution models a common model error is too little detrainment at the freezing level (e.g. Franklin et al. 2013), however, in this convection permitting simulation the change in hydrometeor area with height is mainly due to too little stratiform cloud and rain area, which explains the reduction in area below the melting level and the convective-stratiform modelled ratio being skewed towards more convection than is observed (discussed in section 3.2.2).

A clear difference between the observations and the simulation is the > 20 dBZ reflectivity areas above the freezing level. The observations show some hydrometeors present 1 – 2 km above the freezing level that have reflectivities > 20 dBZ, but no areas that meet the minimum threshold of 5% that have reflectivities > 30 or 40 dBZ. The simulation on the other hand shows large > 20 dBZ fractional areas > 0.6 indicative of larger ice particles in the model than in the observations, which will be explored in detail later. The simulated reflectivity area > 30 dBZ above 5 km is due to the presence of both ice and rain, and the > 40 dBZ areas are almost exclusively due to rain. The simulated rain above the freezing level that is not observed suggests that either the model has faster updrafts than observed, which loft large rain particles upwards and/or the heterogeneous freezing of rain that is not represented in the model is an important process in tropical convection. This latter result is what motivated the experiment with the addition of a heterogeneous rain freezing parameterisation as observations in oceanic convection have shown that most drops freeze between about -6 and -18 °C (Stith et al. 2002, 2004; Heymsfield et al. 2009).

Atmos. Chem. Phys. Discuss., doi:10.5194/acp-2015-970, 2016
Manuscript under review for journal Atmos. Chem. Phys.
Published: 19 January 2016

All simulations show the same main errors in the statistical radar coverage as the control nd case (not shown). The simulation that uses a differing turbulent mixing formulation producing the closest representation of the observed fractional areas for the dBZ thresholds of 10 and 20 dBZ, particularly in the larger areas below the melting level. This can be attributed to the greater detainment between 5 and 8 km at the earlier convective times (see Fig. 5d) due to greater entrainment and mixing of environmental air in this simulation, which acts to increase the amount of IWC (Fig. 3) and the area of precipitation.

3.2.2 Contoured frequency by altitude diagrams

The CPOL contoured frequency by altitude diagrams (CFADs) using the observations from 23 – 24 UTC every 30 minutes exhibits a fairly narrow distribution at the heights above the freezing level, with the altitude range of 12 – 13 km having little variability, reflecting the dominance of small ice particles growing primarily by deposition in the uppermost cloud levels (Figure 7a). Below 10 km the distribution shows increasing reflectivity with decreasing height as particles grow rapidly through aggregation, with reflectivities centred on the modal value of 10 dBZ. At altitudes below the melting level the distribution widens and the reflectivities extend from 5 – 35 dBZ with the largest occurrences around 30 dBZ. The lack of a predominant bright band in the observations may indicate that the particles were heavily rimed rather than aggregated, low density snowflakes due to differences in the dielectric constant and size as these particles melted into rain (e.g. Hogan et al. 2002).

The simulations all show the common errors of: clouds within these reflectivity regions extending too high, reflectivities that are too large between 4 – 6 km, greater reflectivity range below 4 km, and disjointed profiles due to separate hydrometeor categories. The simulations show more of a convective type profile with broader distributions above the freezing level compared to the observations. The more numerous high reflectivity outliers in the simulations indicate a larger number of deep convective cells and/or a smaller proportion of convective – stratiform area.

The simulation with the different dynamical core, ENDGame shown in Figure 7c, shows higher clouds and a broader range of reflectivities at 14 – 16 km. This latter result suggests the presence of large particles being lofted into the upper cloud levels by intense convective cores, as can be seen by the 40 dBZ reflectivities at 17 km. The observations do show some sign of this lofting occurring at 11 – 12 km, however, the reflectivities are constrained to be <

Atmos. Chem. Phys. Discuss., doi:10.5194/acp-2015-970, 2016
Manuscript under review for journal Atmos. Chem. Phys.
Published: 19 January 2016

20 dBZ. This feature can also be seen in the cases that include the ice splintering process, the limited graupel case and the increased droplet number concentration case. The simulations that use the generic ice PSD parameterisation (Fig. 7b and c) overestimate the occurrence of low reflectivities above 10 km and have a modal reflectivity at 6 – 8 km that is too low compared to the observations. Using explicit ice PSDs produces a closer match to the observed reflectivity distribution above 10 km, although the simulated clouds still have greater vertical extent. The modal value of the reflectivities at 6 – 8 km with the explicit PSDs is approximately 15 dBZ, which is greater than the observed value of 10 dBZ.

The inclusion of a heterogeneous rain freezing parameterisation reduces the number of occurrences of reflectivities > 20 dBZ between 5 and 10 km and reduces the cloud top heights. Both of these results agree better with the observations suggesting that this process is important in tropical convective cloud systems. Even in the simulation without graupel the reflectivities are overestimated at the melting level (not shown) and this is due to the ice aggregate PSD. Unlike double moment microphysics schemes, single moment schemes cannot increase the number concentration as the IWC increases and is why the overestimation in reflectivity is seen, even without the contribution from graupel.

Focussing on the 2.5 km reflectivity distribution shown in Figure 8a allows an evaluation of the rain properties from the simulations, in particular the rain DSD. All simulations except for one use the Abel and Boutle (2012) rain DSD, with the remaining simulation testing the sensitivity of rain drop sizes by using the Marshall-Palmer (1948) DSD. The Abel and Boutle rain DSD represents the observed rain reflectivity distribution fairly well, however, the observed peak of 30 dBZ is underestimated and there are too many occurrences in the tails of the distribution. The drier subcloud levels (Fig. 2. and 4) are likely to contribute to the underestimate of the peak reflectivity through enhanced evaporation but cannot explain the larger reflectivities that could result from the stronger convective dynamics as well as the prescribed rain sizes. The contribution from the convective updrafts is demonstrated by the largest occurrences in the high reflectivity tail coming from the simulation with the different dynamical core. It is this ENDGame simulation that produces the strongest updrafts (Fig. 11) and is the least representation of the observed rain reflectivity distribution for the reflectivities > 40 dBZ. The simulation using the Marshall-Palmer DSD peaks at too low a reflectivity at around 10 dBZ and produces too many small rain drops with low reflectivities.

Atmos. Chem. Phys. Discuss., doi:10.5194/acp-2015-970, 2016
Manuscript under review for journal Atmos. Chem. Phys.
Published: 19 January 2016

At 6km the observations again show a single peak reflectivity centred on approximately 15 dBZ (Figure 8b). The simulations show a more complicated distribution at this height with multiple modes due to the presence of multiple hydrometeor species. The simulations that use the generic ice PSD parameterisation peak at -1 dBZ. When this parameterisation is not used and the explicit ice size distribution is used the peak is too high at 24 dBZ. When an additional ice prognostic is added this peak is reduced and compares better to the observations at 18 dBZ, however, the tail of the distribution in these cases is too long with too many occurrences at high reflectivities. While the tail of the distribution for the generic ice PSD cases is also too long, compared to the observed reflectivity distribution these cases represent the graupel reflectivities better than the cases that use the explicit PSD even though all cases use the same graupel PSD. The better graupel representation with the generic ice PSD coupled with the significantly larger occurrence of weak reflectivities around 0 dBZ is similar to the result found by Lang et al. (2011). They modified microphysics parameterisations to reduce the occurrence of excessive large reflectivities and found that this resulted in too many low reflectivities due to a shift in the reflectivity distribution, as is this case here when comparing the generic and explicit ice PSD cases. They suggested that this may be due to entrainment and the sublimation of small ice particles resulting in the observed particle sizes and reflectivities being larger for the low reflectivity end of the distribution than seen in the simulations. This reasoning does not fit this case because the ice sizes from the simulations that use the generic PSD at this height are significantly larger than the simulations with the explicit ice PSD (Fig. 4) and the entrainment from the 3d simulation with the differing turbulent mixing is larger than the other cases that use the generic ice PSD (Fig. 5) yet the reflectivity distribution is very similar suggesting that reduced entrainment is not responsible.

To examine to what extent the generic ice PSD parameterisation is misrepresenting the observed reflectivities or how much the erroneous cloud dynamics are responsible for errors in the modelled reflectivities, the PSD moments derived from the generic PSD parameterisation using the observed IWC and temperature are shown in Figure 9. In calculating the predicted moments the observed mass-diameter relation was used, $m = 4.97 \times 10^{-3} D^{2.05}$, and the observed moments are calculated only for particle sizes > 100 µm in diameter and for IWC > 10^{-3} g m^{-3} to be consistent with the data used to derive the Field et al. (2007) parameterisation. The 4th moment is equivalent to radar reflectivity when mass is proportional to the square of the particle diameter, and it can be seen in Figure 9a that the slope of the parameterised reflectivity results in an overestimate of the larger reflectivities.

Atmos. Chem. Phys. Discuss., doi:10.5194/acp-2015-970, 2016
Manuscript under review for journal Atmos. Chem. Phys.
Published: 19 January 2016

The generic ice PSD parameterisation underestimates the zeroth and first moments and has a good representation of the third moment. The underestimate of the number concentration (Fig. 9d) is consistent with the overestimation of particle sizes and reflectivities. The observations in this case are sampled near convective cores, which is a different type of cloud environment from the data used to construct the Field parameterisation, as demonstrated by the observed number concentration being below the lower range shown in Field et al. (2007).

3.2.3 Maximum reflectivity profiles and vertical velocities

In agreement with many previous studies (e.g. Blossey et al. 2007; Varble et al. 2011) the model overestimates the reflectivity above the freezing level as can be seen in the profiles of maximum reflectivity shown in Figure 10, as well as overestimating the rain reflectivities below 5km. From the set of simulations it can be seen that graupel is not the sole cause of the significantly higher reflectivities as the simulation without graupel also displays this bias. The largest difference between simulated and observed maximum reflectivity during 23 – 24 UTC occurs above 7 km and increases with height for many of the simulations, with the difference between the simulation with the different dynamical core and the observations at 10 km equal to 40 dBZ. The observations show a decrease in the maximum reflectivity with height from approximately 2 km, whereas the simulations tend to show a more constant profile. The observed reduction in height may be due to large raindrops falling out of strong updrafts. The likely overestimate in updraft strength in the simulations (shown next) will advect the raindrops upwards allowing these particles to be collected by the existing ice, generating larger ice particles and maximum reflectivities above the freezing level, as well as acting as a source of latent heating to further fuel convective updrafts. The simulation that decreases the maximum reflectivity with height the most is the simulation with differing subgrid turbulent mixing, which tends to suggest weaker updrafts. The addition of a rain heterogeneous freezing parameterisation follows the different turbulence simulation in reducing the maximum reflectivity from the freezing level up to 8 km, reflecting the reduction in rain and a better representation of the reflectivities.

At 17 – 18 UTC when convection is the strongest in the simulations and the coldest satellite derived cloud top temperatures are observed, the CPOL maximum reflectivity profile has a more constant profile with a slower reduction of reflectivity with height as compared to the later less convective times (Fig. 10). The observed 40 dBZ contour reaches 8 km in agreement with the results of Zipser et al. (2006) who showed that radar echoes of this strength rarely

Atmos. Chem. Phys. Discuss., doi:10.5194/acp-2015-970, 2016
Manuscript under review for journal Atmos. Chem. Phys.
Published: 19 January 2016

occur above 10 km. The profile of maximum reflectivity from the simulation that uses the new dynamical core shows essentially the same profile at these strong convective times as for the later times when the MCS has matured, unlike the observations and the majority of the simulations, suggesting that there is less variability in maximum updraft when using ENDGame. There is little spread in the maximum reflectivity profile across the simulations at 17 – 18 UTC, with the clear difference in the two simulations that limit or exclude graupel, demonstrating that at the time of strongest convection, the vertical advection of graupel is responsible for the largest error in the maximum reflectivities in the upper troposphere.

Comparing the control case with the cases that use a different dynamical core and different turbulent mixing parameterisation shows that the reduction in maximum reflectivity with height at 23 – 24 UTC is well correlated with the reduction in maximum vertical velocity shown in Figure 11c. These cases all use the generic ice PSD and the differences are likely due to the different entrainment and water loading that affects the cloud buoyancy and the strength of the updrafts that advect large particles into the upper troposphere. The ENDGame simulation produces significantly larger maximum updrafts and has less accumulated ice water (see Fig. 16), and conversely there is greater accumulated IWC for the simulation with the different turbulent mixing parameterisation compared to the control case and associated lower maximum vertical velocities and maximum reflectivities.

Comparing the differences in maximum vertical velocity across the simulations for the times 23 – 24 UTC shows that the largest sensitivity tends to come from the choice of dynamics and turbulence. The reduction in updraft strength at these times with the 3D Smagorinsky turbulence scheme is also achieved with the inclusion of a rain heterogeneous freezing parameterisation. Both of these cases tend to have larger ice water contents in strong updrafts (see Fig. 12) that will reduce buoyancy through the effect of water loading. While there is different sampling between the aircraft observations and the simulations, the aircraft observations of maximum updraft strength shown in Figure 10 are smaller than the ENDGame simulation by as much as 20 m s^{-1}. In this simulation the stronger and deeper updrafts are able to generate enough latent heating that this effect on buoyancy is larger than that of entrainment and water loading as compared to the other cases. The in-cloud mean vertical velocity for this simulation is also larger than the other cases from 4 – 8 km, as well as the 99th percentile of upward vertical motion (Figure 11). The shape of the mean updraft velocity is similar for the ENDGame case and the simulation without graupel, both showing

Atmos. Chem. Phys. Discuss., doi:10.5194/acp-2015-970, 2016
Manuscript under review for journal Atmos. Chem. Phys.
Published: 19 January 2016

greater mean updraft strength from cloud base to 6 – 7 km. These two simulations produce the largest domain mean rain rate (Fig. 3a) at these times and show that dynamical changes to the cloud system can be achieved through changes to the model's dynamical core and the cloud microphysics.

While the maximum updrafts produced by the simulations at these times are within the range of observed maximum tropical updrafts from other field campaigns at Darwin (e.g. < 25 m s^{-1} in TWP-ICE; Varble et al. 2014a), the maximum updrafts produced throughout the MCS lifecycle are much larger and in excess of 50 m s^{-1} for the ENDGame simulation at 17 – 18 UTC. These values are well outside the range of maximum vertical velocities presented for oceanic convection by Heymsfield et al. (2010) and agree with other studies showing excessive tropical vertical velocities simulated by convection permitting models (e.g Varble et al. 2014a).

The control simulation shows a large peak in the mean upwards vertical velocity and the 99th percentile at cloud base at approximately 3 km (Fig. 11). The in-cloud velocity statistics are calculated where cloud and/or ice water is present but does not include rain areas, and hence the peak in updraft strength at cloud base is associated with the buoyancy production generated by the condensation and latent heating of air that reaches saturation. Most of the simulations show a double peak in vertical velocities with maxima at cloud base and in the upper troposphere at about 13 km. The upper level updraft peak has been observed (e.g. May and Rajopadhyaya 1999) and is argued to be due to latent heat released by freezing condensate and the unloading of hydrometeors, both of which increase parcel buoyancy. A bimodal peak has been observed but tends to be correlated with the freezing level and not cloud base as seen in the simulations. The apparent lack of observational support for the cloud base peak is likely due to the inability of many observations to distinguish between non-precipitating cloud and clear air, and dual profiler measurements during TWP-ICE do show some evidence of a cloud base peak (Collis et al. 2013).

3.3 Phase composition and comparison with in situ observations

In the simulations the relationship of IWC to vertical velocity changes with the temperature regime, as shown in Figure 12. For the warmest range of 0 to -5 °C the IWC reduces as the strength of the updraft increases from 1 m s^{-1}. For the two intermediate temperature regimes, -5 to -10 and -10 to -20 °C, the IWC is fairly constant with vertical velocities greater than 2 m

Atmos. Chem. Phys. Discuss., doi:10.5194/acp-2015-970, 2016
Manuscript under review for journal Atmos. Chem. Phys.
Published: 19 January 2016

Atmospheric Chemistry and Physics Discussions

s^{-1}, with the colder regime consisting of 1 g m^{-3} more ice for a given vertical velocity. For the coldest regime analysed the IWC increases as the vertical velocity increases. For the warmest temperature regime the decline of IWC with updraft speed is offset by the strong increase in LWC, with the fraction of condensate that is supercooled cloud water reaching 0.8 at 15 m s^{-1} (Fig.13). In this temperature regime there is no new ice being formed as heterogeneous freezing in the model does not occur until the temperature cools to -10 °C. Any ice in this regime has formed above and has been recirculated into these updrafts, and as the vertical velocity increases the saturation specific humidity increases faster than the supercooled water can be removed by deposition and riming resulting in the large LWC. The circulation of ice from high levels to those below was suggested by Black and Hallett (1999) to be a factor in the observed rapid glaciation of clouds in hurricanes. The no graupel and limited graupel cases do not show the same decline in IWC. For these cases the fraction of condensate that is supercooled water is lower so there is less competition for the available water vapour, which results in greater depositional ice growth. In these simulations the greater proportion of ice particles with slower fall speeds leads to greater in-cloud residence times producing larger accumulated IWC than the other cases with two ice prognostics (see Fig. 16). This shows that when graupel is included in the simulations and allowed to grow unrestricted, the removal of LWC by ice processes is less efficient in this temperature regime. The other simulation with different behaviour and larger IWC is the case that includes rain heterogeneous freezing. In this simulation there is an additional source of ice and this results in greater IWC in strong updrafts due to the rain that is advected upwards freezing rather than remaining as liquid water as in the other simulations. The impact of this on the cloud liquid water is to increase the cloud water content in strong updrafts as shown in Figure 13. This is due to the reduction in the accretion of cloud water by rain given the reduced rain water content.

The large IWC in the downdraft regions of the warmer temperature regime is where graupel is expected, which is often located behind and below the convective updrafts (Barnes and Houze 2014) where the suggestion is that the fast fall speeds of these larger particles help to generate downdrafts (Franklin et al. 2005; Jung et al. 2012). This argument is supported by Figure 16 that shows that the simulations with the largest accumulated graupel mass tend to be the simulations with the largest IWC in the downdrafts. The colder regime of -10 to -5 °C shows IWC invariable to vertical velocity. These colder temperatures will produce a greater difference in saturated vapour pressure and saturated vapour pressure over ice and, therefore, larger depositional growth rates via the Bergeron-Findeisen process than the warmer

Atmos. Chem. Phys. Discuss., doi:10.5194/acp-2015-970, 2016
Manuscript under review for journal Atmos. Chem. Phys.
Published: 19 January 2016

temperature regime. There are few observations within the -10 – 0 °C regimes (Figure 12e), however, the observed IWC for vertical velocities between 0 and -2 m s^{-1} shows broad agreement with the simulations with an average IWC of 0.5 g m^{-3}.

For the temperature regime of -20 to -10 °C there is a small increase in IWC with vertical velocity (Fig. 12c) due to the effects of heterogeneous freezing on increasing the mass of ice and further increases in the vapour pressure. The simulations show fairly good agreement with the observations across the velocities -1 – 2 m s^{-1}, with the mean IWC ranging from 0.5 – 2 g m^{-3}. The observed IWC then drops off but increases again to be equal to 2.4 g m^{-3} for updrafts of 15 m s^{-1}. The reduction in observed IWC seems likely to be due to sampling. For updrafts greater than 10 m s^{-1} there is a large range of variability across the simulations and all are typically within one standard deviation of each other.

For the coldest temperature regime sampled by the aircraft, -30 to -20 °C, the observations show an increase in IWC as the strength of the downdraft intensifies to -3 m s^{-1} (Fig. 12d), as what is simulated for all temperature regimes. The downdraft IWC of 0.2 – 1 g m^{-3} is in reasonable agreement with the simulations and particularly for the simulation that has the additional ice prognostic variable, where the IWC does not monotonically increase with downdraft strength. Comparing the observed IWC for the two colder regimes shows a decrease in IWC at the colder temperatures, for example IWC is about 2 g m^{-3} at 2 m s^{-1} for the -20 - -10 °C regime and only 1 g m^{-3} in the colder regime. The simulations capture this result and show that the reason may be due to the reduction in supercooled liquid water at the colder temperatures (Fig.14), suggesting that this is an important source for ice particle growth in this simulated case. The spread in IWC across the simulations is typically not statistically significant, particularly for the stronger updrafts, however, the differences can be attributed to the effects that the changes have on producing and removing LWC, with different dynamics, turbulence and microphysics all displaying sensitivities to the amount and distribution of IWC within tropical clouds.

Across the four temperature regimes all of the simulations show an increase in cloud LWC with updraft strength, with the LWC reducing as the temperature cools along with the fraction of condensate that is supercooled liquid water as shown in Figures 13 and 14. The strongest updrafts are associated with convective cores that will have minimal entrainment and consequently high supersaturations. Note that we include only cloud water in these figures, rather than cloud and rain, as it is only the cloud water that is used in the growth of ice via the

Atmos. Chem. Phys. Discuss., doi:10.5194/acp-2015-970, 2016
Manuscript under review for journal Atmos. Chem. Phys.
Published: 19 January 2016

Bergeron-Findeisen process and allowed to heterogeneously freeze in the model. Including rain water increases the LWC and the variance across the simulations for the warmer regimes but does not change the main conclusions regarding ice growth. Also note that the cloud water contents for the warmest temperature regime agree reasonably well with those presented in Table 3 of Heymsfield and Willis (2014). Between -10 and -5 °C the fraction of condensate that is supercooled water reduces significantly compared to the warmer regime, however, the mass of cloud water stays the same. Hence the control on the amount of cloud water that occurs between -10 and 0 °C is the updraft strength and not the temperature, due to heterogeneous freezing not occurring until the temperatures cool to -10 °C and below. The simulations that use the generic ice PSD tend to have lower liquid water contents for a given vertical velocity, likely due to the increased accretion and riming growth due to the larger ice particle sizes compared to the explicit PSD (Fig. 4 and 17). This result continues to be seen for the colder temperature regimes shown in Figure 14.

Increasing the cloud droplet number concentration in the model only directly impacts the microphysical process of autoconversion between cloud droplets and rain, and reduces the precipitation efficiency. For this case the reduced autoconversion rate does not make a significant difference to the surface rainfall, since the ice processes dominate the rainfall production (see Fig. 3). However, the less efficient transfer of cloud water mass to rain does change the cloud structure with more LWC and a larger fraction of condensate being supercooled water for the temperatures between -10 and -30 °C, with the difference between the other simulations increasing with the strength of vertical motion. As cloud water is the only liquid water source used in the model for deposition growth via the Bergeron-Findeisen mechanism and that can freeze heterogeneously, this implies potentially greater growth rates for ice and stronger updrafts through enhanced latent heating; the so-called aerosol invigoration effect (Rosenfeld et al. 2008). While it is not clear from Figure 12 that this is the case, Figure 16 shows that the accumulated amount of aggregate mass is actually less in this simulation with enhanced droplet number concentration, however, this case generates the greatest mass of graupel. This shows that the larger mass of cloud water increases the riming by aggregates and thus the production of graupel, which results in a reduction in the total accumulated ice mass, possibly due to depositional growth of graupel not being included in the model.

Atmos. Chem. Phys. Discuss., doi:10.5194/acp-2015-970, 2016
Manuscript under review for journal Atmos. Chem. Phys.
Published: 19 January 2016

Atmospheric Chemistry and Physics Discussions

The other simulation that produces more cloud water for updrafts > 5 m s^{-1} in the coldest temperature regime is the simulation that includes ice splintering or the Hallet-Mossop process (Fig. 14). Looking at the accumulated ice crystal mass between the simulation that does and does not include an ice splintering parameterisation (qcf2 and qcf2hm) shows that while there tends to be less crystal mass at most heights when the H-M process is included, there are crystals present in updrafts up to 15 m s^{-1}, whereas in the qcf2 case there are no crystals present in updrafts > 4 m s^{-1} (not shown). Similarly for the aggregates there is ice spread across a wider range of updrafts when the H-M process is included, particularly for the colder temperatures, resulting in a larger accumulated amount of snow and total ice (Fig. 16). The generation of a larger quantity of ice crystal mass in the H-M zone allows for a larger amount to be transported to the upper cloud levels by the convective updrafts where the crystals then grow through deposition, riming and aggregation producing a larger mass of snow. The increased latent heating in the H-M zone does produce a slightly larger 90^{th} percentile cloud updraft velocity (Fig. 11). This increase in the number and/or strength of updrafts supports the transport of more liquid water in the case with the ice splintering parameterisation, which also helps to increase the IWC.

The in-cloud relative humidity is less variable as a function of updraft strength for the warmer temperature regimes in both the observations and the simulations (Fig. 15). The increase in RH as the vertical velocity increases for the colder temperature regimes is seen in the observations and simulations for the low updraft speeds, however, for the stronger updrafts the model either flattens off or continues to increase while the observations reduce the RH. This likely reflects the aircraft sampling and is seen in the IWC as well (Fig 12). Compared to the simulations, the higher RH for the temperature regime of -20 to -10 °C in the observations for the updrafts greater than 10 m s^{-1} coincides with less IWC in the observations and more in the simulations. This result suggests that the model is too efficient in reducing supersaturation and growing ice particles through deposition. An additional experiment was performed to test the reduction in capacitance due to an axial ratio not equal to one (i.e. non-spherical particles). This reduction in the depositional growth rate did reduce the IWC (the total accumulated ice reduced by 5%) particularly in the strongest updrafts with the largest supersaturations, however, the RH did not appreciably increase (not shown). This is the opposite result found by Furtado et al. (2014) who found little effect on IWC and instead found a significant change in RH, probably reflecting the differing dynamical situations of the two studies, with their cases being steady state ice only clouds.

Atmos. Chem. Phys. Discuss., doi:10.5194/acp-2015-970, 2016
Manuscript under review for journal Atmos. Chem. Phys.
Published: 19 January 2016

The observed characteristic ice size (mean mass weighted diameter) shown in Figure 17 increases with warmer temperatures and shows a strong dependence on IWC, with the characteristic size decreasing with increasing IWC reflecting the dominance of smaller particles for higher IWC. This contrasts with the lack of dependence of mean ice particle size on IWC that has been observed in earlier flights over Darwin and Cayenne in 2010 – 2012 (Fridlind et al. 2015) but agrees with more recent findings by Leroy et al. (2015). The modelled mean snow diameter increases with increasing temperature, reflecting the process of aggregation, however, the modelled snow PSD also increases the mean diameter with increasing IWC with the rate of increase being similar in both the generic ice PSD and the explicit specified gamma size distribution. The mean diameter from the generic ice PSD tends to agree well with the observed size for IWC < 0.5 g m^{-3}, however, the sizes are significantly overestimated for IWC > 0.5 g m^{-3}. Given that the number concentration is dependent on the size of the particles for a given IWC, this implies that the generic ice PSD simulates smaller concentrations of larger particles for a given IWC than the observations as shown previously in Figure 9. This reflects the data that was used to develop the generic ice PSD coming largely from stratiform clouds with smaller IWC and larger ice particles. The explicit gamma PSD shows the opposite behaviour, underestimating the mean ice diameter for IWC < 0.5 g m^{-3} and matching the observed size for higher IWC. To be able to correctly represent the snow sizes in the model for this case requires a bimodal PSD parameterisation or the use of a wider data set that includes high IWC observations to generate a more applicable generic ice PSD parameterisation for modelling tropical convective cloud systems.

4 Conclusions

A set of 1 km horizontal grid length simulations has been analysed to evaluate the ability of the UM to simulate tropical convective cloud systems and to investigate the impacts of different dynamical, turbulent and microphysical representations on the phase composition and ice water contents. The case study is for February 18 2014 where active monsoon conditions produced a mesoscale convective system in the Darwin area. The simulations reproduce the observed deep westerly winds that are the source of moisture for the long-lived cloud system, however, the simulations are too warm and dry below the freezing level and too warm and moist above this level, particularly in the upper troposphere. The simulation with the differing dynamical core is the least representative of the observed sounding, with the

Atmos. Chem. Phys. Discuss., doi:10.5194/acp-2015-970, 2016
Manuscript under review for journal Atmos. Chem. Phys.
Published: 19 January 2016

most accurate being the simulation with an additional ice prognostic and heterogeneous rain freezing parameterisation.

Analysing 12 hours of observed and simulated radar reflectivity has shown that the simulations capture the intensification and decay of convective strength associated with the lifecycle of the MCS, with the timing of the deepest convection represented well. However, the radar detectable cloud tops heights are overestimated by the simulations, as are the maximum reflectivities and areas above the freezing level with reflectivities greater than 30 dBZ. The observed maximum domain averaged precipitation rate coincides with the generation of significant anvil cloud, whereas the simulations generate the highest mean precipitation rate a few hours too early at the times of deepest convection. Aircraft observations of maximum vertical velocity suggest that the new dynamical core simulation overestimates the strength of convection at the mature-decaying stage of the MCS. In this case the stronger updrafts contribute to the excessive reflectivities above the freezing level, but this was apparent in all of the simulations albeit to a lesser degree, suggesting that both the updraft dynamics and the particle sizes are responsible for this error. These strong convective updrafts will loft condensate, including large particles, into the upper troposphere where their subsequent freezing will release latent heat that will further drive the simulated updrafts. In the observed reflectivity distribution there is evidence of the lofting of large particles up to 12 km, which is captured by a number of the simulations although the heights are above 15 km and the reflectivities larger than those observed by up to 20 dBZ.

The simulated reflectivity CFADs show more of a convective type profile compared to the observations, with broader distributions and a greater occurrence of high reflectivity outliers that suggests a larger number of convective cells in the simulations. The simulation with the differing turbulence parameterisation showed the best agreement with the observed maximum reflectivity at the later times of 23 – 24 UTC. The change to the 3D Smagorinsky scheme induces greater mixing and more dilute convective plumes resulting in a reduction of the maximum vertical velocities and reflectivities. This same reduction in the vertical velocity and reflectivity up to 8 km was also found with a change to the microphysics formulation with the addition of a rain heterogeneous freezing parameterisation. At 17 – 18 UTC at the time of deepest convection, all simulations showed a similar error in maximum reflectivity regardless of dynamics or turbulence formulation, and in fact the 3D Smagorinsky scheme produced the fastest 90th percentile updraft speed. The largest sensitivities in the maximum updraft

Atmos. Chem. Phys. Discuss., doi:10.5194/acp-2015-970, 2016
Manuscript under review for journal Atmos. Chem. Phys.
Published: 19 January 2016

velocities are generally produced by changes to the dynamical and turbulence formulations in the model. However, the spread across the simulations for the mean and percentiles of updraft velocity show the greatest sensitivity coming from changes to the microphysical parameters and processes. Changing the microphysics affects the dynamics by altering the vertical distribution of latent heating, which drives the vertical motions. The horizontal mass divergence and convective updraft buoyancy was shown to be most sensitive to the turbulence parameterisation in the mixed-phase regions of the updrafts, where the greater mixing generated larger entrainment and a greater detrainment of mass at these heights. The upper ice-only regions of the convective updrafts showed that the control on updraft buoyancy was the sizes of the ice particles with smaller particles reducing updraft buoyancy and limiting the cloud top heights, reflecting the importance of the microphysical processes on the convective dynamics.

The simulations that use an explicit ice PSD rather than the generic PSD parameterisation produce greater occurrences of larger reflectivities that more closely resemble the observations, although the modal reflectivity is overestimated. The reflectivity distributions as a function of height do not show the same slope with altitude when comparing the observations to the simulations using the generic ice PSD. Given that at the heights of 6 – 9 km the domain is almost completely covered by hydrometeors, this suggests that for the majority of occurrences the temperature dependency in the generic ice PSD and the implicit representation of aggregation is too weak. This can also be seen in the comparison of the particle mean diameters with the in situ observations where the explicit PSD for an IWC of 0.5 g m^{-3} increases by about 2.6 times from the coolest to the warmest regime, while the generic ice PSD increases by 1.6 and the observations show more than a tripling in mean size. The beneficial impact of including a rain heterogeneous freezing parameterisation was shown through the reduction of large raindrops being advected above the freezing level, which was not observed by the radar or aircraft during the mature stage of the MCS and supports previous observations that show that most drops in oceanic convection freeze between -6 and -18 °C (Stith et al. 2002). The simulation without graupel also overestimates the reflectivities at the melting level demonstrating that it is not only graupel that causes excessively large reflectivities but also snow in simulations that use a single moment microphysics scheme.

Analysing the relationship between phase composition and vertical velocity for 4 different temperature regimes shows that the LWC increases with increasing updraft strength, and as

Atmos. Chem. Phys. Discuss., doi:10.5194/acp-2015-970, 2016
Manuscript under review for journal Atmos. Chem. Phys.
Published: 19 January 2016

the temperature cools the LWC reduces along with the fraction of condensate that is supercooled liquid water. With increasing ascent the rate that the saturation specific humidity is lowered is increasingly faster than the rate that the liquid water can be reduced by deposition and riming of ice, resulting in an increase of LWC with vertical velocity. For the warmest temperature regimes the simulations with no or restricted graupel growth produced the greatest amount of IWC and lowest LWC for vertical velocities greater than 7 m s^{-1}. Ice in these regimes with temperatures > -10 °C has formed above and has been recirculated into these updrafts. The perturbed graupel cases have a larger amount of mass contained in the slower falling snow particles and this results in a more efficient removal of LWC through increased in-cloud residence time and an increase in the accumulated ice water content.

The simulations show that the growth of liquid drops is more sensitive to the vertical velocity than the growth of ice particles, as has been documented previously (Korolev 2008). For the colder temperature regimes the simulations that use the explicit ice PSD rather than the generic ice PSD parameterisation tend to have more LWC, which is probably due to the reduced accretion and riming rates associated with the smaller particles. The three simulations that tended to produce more LWC for a given updraft strength for the colder regimes are the simulations with an increased cloud droplet number concentration, inclusion of an ice splintering parameterisation and inclusion of a heterogeneous rain freezing parameterisation. Increasing the cloud droplet number concentration reduces the precipitation efficiency of warm rain processes and generates more cloud water and a greater fraction of condensate being supercooled liquid water for temperatures between -10 and -30 °C. In the model cloud water is the only liquid water used for depositional growth via the Bergeron-Findeisen mechanism and heterogeneous freezing, and the increased cloud water in this simulation produces the largest accumulation of graupel. Including a parameterisation of the secondary ice production Hallett-Mossop process that increases the deposition rate generates a larger quantity of ice, which through the increased latent heating supports the transport of more cloud liquid water and allows ice crystals and aggregates to be present across a wider range of updraft speeds. The other simulation with different behaviour and larger cloud LWC is the case that includes rain heterogeneous freezing. The impact of including this process in the model is to increase the cloud water content in strong updrafts due to the reduction in the accretion of cloud water by rain given the reduced rain water content.

The evaluation of a tropical mesoscale convective system in this study has documented a number of model shortcomings and developments that improve the model performance:

1. Excessive areas with high reflectivities improve with reduced ice sizes, inclusion of a heterogeneous freezing rain parameterisation, an additional ice prognostic variable and increased turbulent mixing through the use of the 3D Smagorinsky turbulence scheme.
2. Too much rain above the freezing level is reduced with the inclusion of a heterogeneous rain freezing parameterisation.
3. Too little entrainment is increased with smaller ice sizes and increased turbulent mixing, which increases the stratiform cloud and rain area.
4. Too efficient depositional growth of ice is improved with a reduction in depositional capacitance that includes the effects of non-spherical ice particles.

While the listed model changes do improve aspects of the simulations, none of these produce a simulation that closely matches all of the observations. This study has shown the need to include a better representation of the observed bimodal ice size distribution, which would impact the model's representation of the ice water contents and reflectivities, as well as the convective dynamics through the effects of latent heating and water loading on buoyancy.

Acknowledgements

This research has received funding from the Federal Aviation Administration (FAA), Aviation Research Division, and Aviation Weather Division, under agreement CON-I-2901 with the Australian Bureau of Meteorology. The research was also conducted as part of the European Union's Seventh Framework Program in research, technological development and demonstration under grant agreement n°ACP2-GA-2012-314314, and the European Aviation Safety Agency (EASA) Research Program under service contract n° EASA.2013.FC27. Funding to support the development and testing of the isokinetic bulk TWC probe was provided by the FAA, NASA Aviation Safety Program, Environment Canada, and the National Research Council of Canada. Funding for the Darwin flight project was provided by the EU Seventh Framework Program agreement and EASA contract noted above, the FAA, the NASA Aviation Safety Program, the Boeing Co., Environment Canada, and Transport Canada. We acknowledge use of the MONSooN system, a collaborative facility supplied under the Joint Weather and Climate Research Programme, which is a strategic partnership

between the Met Office and the Natural Environment Research Council. We would like to express our thanks to Stuart Webster and Adrian Hill for providing the control model configuration, and to Paul Field for suggesting the analysis presented in Figure 9. The satellite data were provided by the NASA Langley group led by Pat Minnis.

References

Abel, S. and I.A. Boutle, 2012: An improved representation of the rain drop size distribution for single-moment microphysics schemes, *Q. J. Roy. Meteor. Soc.*, **138**, 2151-2162

Abel, S. and B.J. Shipway, 2007: A comparison of cloud-resolving model simulations of trade wind cumulus with aircraft observations taken during RICO. *Q. J. R. Meteorol. Soc.*, **133**, 781 – 794

Barnes, H.C and R.A. Houze Jr., 2014: Precipitation hydrometeor type relative to mesoscale airflow in mature oceanic deep convection of the Madden-Julian Oscillation. *J. Geophys. Res. Atmos.*, doi: 10.1002/2014JD022241

Baumgardner, D., et al., 2001. The cloud, aerosol and precipitation spectrometer (CAPS): a new instrument for cloud investigations. *Atmos. Res.*, **59–60**, 251–264

Black, R. and J. Hallett, 1999: Observations of the distribution of ice in hurricanes. *J. Atmos. Sci.*, **43**, 802 – 822

Bigg, E.K., 1953: The supercooling of water. *Proc. Phys. Soc. London*, **B66**, 688-694

Blossy, P.N., C.S. Bretherton, J. Cetrone and M. Kharoutdinov, 2007: Cloud-resolving model simulations of KWAJEX: Model sensitivities and comparisons with satellite and radar observations. *J. Atmos. Sci.*, **64**, 1488 – 1508

Boutle, I.A. J.E.J. Eyre and A.P. Lock, 2014: Seamless stratocumulus simulation across the turbulent gray zone. *Mon. Wea. Rev.*, **142**, 1655 - 1668

Bretherton, C.S., P.N. Blossey and M. Khairoutdinov, 2005: An energy-balance analysis of deep convective self-aggregation above uniform SST. *J. Atmos. Sci.*, **62**, 4273 – 4292

Cardwell, J.R., T.W. Choularton, D. Wilson and R. Kershaw, 2002: Use of an explicit model of the microphysics of precipitating stratiform cloud to test a bulk microphysics scheme. *Q. J. R. Meteorol. Soc.*, **128**, 573 – 592

Clark, A. J., W. A. Gallus, and T.-C. Chen, 2007: Comparison of the diurnal precipitation cycle in convection-resolving and non-convection-resolving mesoscale models, *Mon.Wea. Rev*., **135**, 3456–3473

Collis, S., A. Protat, P.T. May and C. Williams, 2013: Statistics of storm updraft velocities from TWP-ICE including verification with profiling measurements. *J. App. Meteor.*, **52**, 1909 – 1922

Cox, G.P., 1988: Modelling precipitation in frontal rainbands. *Q. J. R. Meteorol. Soc.*, **114**, 115 – 127

Davies, T., M.J.P. Cullen, A.J. Malcolm, M.H. Mawson, A. Staniforth, A.A. White and N. Wood, 2005: A new dynamical core for the Met Office's global and regional modelling of the atmosphere. *Q. J. R. Meteorol. Soc.*, **131**, 1759 – 1782

Davison, C. R., J.D. MacLeod, and J.W. Strapp, 2009: Naturally Aspirating Isokinetic Total Water Content Probe: Evaporator Design and Testing. *1st AIAA Atmospheric and Space Environments*, June 25, 2009, San Antonio, Texas, AIAA-2009-3861.

Del Genio, A.D. and J. Wu, 2010: The role of entrainment in the diurnal cycle of continental convection. *J. Clim.*, **23**, 2722-2738

Edwards, J.M. and A. Slingo, 1996: Studies with a new flexible radiation code. I: Choosing a configuration for a large-scale model. *Q. J. R. Meteorol. Soc.*, **122**, 689 – 720

Fein, J.S. and P.L. Stephens, 1987: *Monsoons*. Wiley, 632pp.

Ferrier, B.S., 1994: A double-moment multiple-phase four-class bulk ice scheme. Part I: Description. *J. Atmos. Sci.*, **51**, 249 – 280

Field, P.R., A.J. Heymsfield and A. Bansemer, 2007: Snow size distribution parameterisation for midlatitude and tropical ice clouds. *J. Atmos. Sci.*, **64**, 4346 – 4365

Fletcher, N.H., 1962: *The Physics of Rain Clouds*. Cambridge University Press, 386 pp.

Franklin, C.N., G.J. Holland and P.T. May, 2005: Sensitivity of tropical cyclone rainbands to ice-phase microphysics. *Mon. Weather Rev.*, **133**, 2473 – 2493

Franklin, C.N., Z. Sun, D. Bi, M. Dix, H. Yan and A. Bodas-Salcedo, 2013: Evaluation of clouds in ACCESS using the satellite simulator package COSP: Global, seasonal and regional cloud properties. *J. Geophys. Res. Atmos.*, **118**, 732 – 748

Fridlind, A.M., A.S. Ackerman, J.-P. Chaboureau, J. Fan, W.W. Grabowski, A.A. Hill, T.R. Jones, M.M. Khaiyer, G. Liu, P. Minnis, H. Morrison, L. Nguyen, S. Park, J.C. Petch, J.-P. Pinty, C. Schumacher, B.J. Shipway, A.C. Varble, X. Wu, S. Xie and M. Zhang, 2012: A comparison of TWP-ICE observational data with cloud-resolving model results. *J. Geophys. Res. Atmos.*, **117,** D05204, doi:10.1029/2011JD016595

Fridlind, A.M., A.S. Ackerman, A. Gandin, F. Dezitter, M. Weber, J.W. Strapp, A. V. Korolev and C.R. Williams, 2015: High ice water content at low radar reflectivity near deep convection – Part 1: Consistency of in situ and remote-sensing observations with stratiform rain column simulations. *Atmos. Chem. Phys. Discuss.*, **15**, 16505 - 16550

Furtado, K., P.R. Field, R. Cotton and A.J. Baran 2014: The sensitivity of simulated high clouds to ice crystal fall speed, shape and size distribution. *Q. J. R. Meteorol. Soc.*, doi:10.1002/qj.2457

Gregory, D. and P.R. Rowntree, 1990: A mass flux convection scheme with representation of cloud ensemble characteristics and stability-dependent closure. *Mon. Wea. Rev.*, **118**, 1483-1506

Hallett, J. and S.C. Mossop, 1974: Production of secondary ice particles during the riming process. *Nature*, **249**, 26 – 28

Heymsfield, A.J., A. Bansemer, G. Heymsfield and A.O. Fierro, 2009: Microphysics of maritime tropical convective updrafts at temperatures from -20° to -60°. *J. Atmos. Sci.*, **66**, 3530 – 3562

Heymsfield, A.J. and P. Willis, 2014: Cloud conditions favouring secondary ice particle production in tropical maritime convection. *J. Atmos. Sci.*, **71**, 4500 - 4526

Heymsfield, G.M., L. Tian, A.J. Heymsfield, L. Li and S. Guimond, 2010: Characteristics of deep tropical and subtropical convection from nadir-viewing high-altitude airborne Doppler radar. *J. Atmos. Sci.*, **67**, 285 – 308

Hogan, R.J., P.R. Field, A.J. Illingworth, R.J. Cotton and T.W. Choularton, 2002: Properties of embedded convection in warm-frontal mixed-phase cloud from aircraft and polarimetric radar. *Q. J. R. Meteorol. Soc.*, **128**, 451 – 476

Hogan, R.J., M.P. Mittermaier and A.J. Illingworth, 2006: The retrieval of ice water content from radar reflectivity factor and temperature and its use in evaluating a mesoscale model. *J. Appl. Meteorol.*, **45**, 301 - 317

Houze, R.A., P.V. Hobbs, P.H. Herzegh and D.B. Parsons, 1979: Size distributions of precipitation particles in frontal clouds. *J. Atmos. Sci.*, **36**, 156 – 162

Jung, S.-A., D.-I. Lee, B. Jou and H. Uyeda, 2012: Microphysical properties of maritime squall line observed on June 2, 2008 in Taiwan. *Journal of the Meteorological Society of Japan*, **90**, 813-250

Keenan, T.D., K. Glasson, F. Cummings, T.S. Bird, J. Keeler and J. Lutz, 1998: The BMRC/NCAR C-band polarimetric (C-POL) radar system. *J. Atmos. Oceanic Technol.*, **15**, 871 - 886

Korolev, A.V., 2008: Rates of phase transformations in mixed-phase clouds. *Q. J. R. Meteorol. Soc.*, **134**, 595 – 608

Lang, S.E., W.-K. Tao, X. Zeng and Y. Li, 2011: Reducing the biases in simulated radar reflectivities from a bulk microphysics scheme: Tropical convective systems. *J. Atmos. Sci.*, **68**, 2306 – 2320

Lawson, R. P., L. J. Angus, and A. J. Heymsfield, 1998: Cloud particle measurements in thunderstorm anvils and possible threat to aviation, J. Aircraft, 35(1), 113-121

Lawson, R. P., D. O'Connor, P. Zmarzly, K. Weaver, B. A. Baker, Q. Mo, and H. Jonsson, 2006: The 2D-S (Stereo) probe: Design and preliminary tests of a new airborne, high speed, high-resolution particle imaging probe, *J. of Atmos. Oceanic Technol.*, **23**, 1462-1477

Leroy, D., E. Fontaine, A. Schwarzenboeck, J.W. Strapp, L. Lilie, J. Delanoë, A. Protat, F. Dezitter and A. Grandin, 2015: HAIC/HIWC field campaign-specific findings on PSD microphysics in high IWC regions from in situ measurements: Median mass diameters, particle size distribution characteristics and ice crystal shapes. Tech. Rep. 2015-01-2087, SAE International, Warrendale, PA, USA, doi:10.4271/2015-01-2087

Liu, G. and J. Curry, 1999: Remote sensing of ice water characteristics in tropical clouds using aircraft microwave measurements. *J. App. Meteor.*, **37**, 337 – 355

Lock, A.P., A.R. Brown, M.R. Bush, G.M. Martin and R.N.B. Smith, 2000: A new boundary-layer mixing scheme. Part I: Scheme description and single-column model tests. *Mon. Weather Rev.*, **128**, 3187 – 3199

Marshall, J.S. and W.M.K. Palmer, 1948: The distribution of raindrops with size. *Journal of Meteorology*, **5**, 165 – 166

Mason, J. G., J. W. Strapp, and P. Chow, 2006: The ice particle threat to engines in flight. 44th AIAA Aerospace Sciences Meeting, Reno, Nevada, 9-12 January 2006, AIAA-2006-206. Available online at http://arc.aiaa.org/doi/abs/10.2514/6.2006-206

May, P.T. and T. Lane, 2009: A method for using weather radar data to test cloud resolving models. *Meteorological Applications*, **16**, 425 – 432

May, P.T. and D.K. Rajopadhyaya, 1999: Vertical velocity characteristics of deep convection over Darwin, Australia. *Mon. Weather Rev.*, **127**, 1056 – 1071

McBeath, K., P.R. Field and R.J. Cotton, 2014: Using operational weather radar to assess high-resolution numerical weather prediction over the British Isles for a cold air outbreak. *Q. J. R. Meteorol. Soc.*, **140**, 225 – 239

Minnis, P. and W.L. Smith Jr., 1998: Cloud and radiative fields derivedfrom GOES-8 during SUCCESS and the ARM-UAV spring 1996 flight series, *Geophys. Res. Lett.*, **25,** 1113–1116.

Minnis, P. et al. 2008: Cloud detection in non-polar regions for CERES using TRMM VIRS and Terra and Aqua MODIS data, IEEE Trans. *Geosci. Remote Sens*., **46**, 3857–3884.

Minnis, P., et al. 2011: CERES Edition 2 cloud property retrievals using TRMM VIRS and Terra and Aqua MODIS data–Part I: Algorithms, *IEEE Trans. Geosci. Remote Sens*., **11**, 4374–4400, doi:10.1109/TGRS.2011.2144601.

Mitchell, D.L., 1996: Use of mass- and are-dimensional power laws for determining precipitation particle terminal velocities. *J. Atmos. Sci.*, **53**, 1710 – 1722

Morrison, H., G. Thompson and V. Tatarskii, 2009: Impact of cloud microphysics on the development of trailing stratiform precipitation in a simulated squall line: Comparison of one- and two-moment schemes. *Mon. Weather Rev.*, **137**, 991 – 1007

Puri, K. et al, 2013: Implementation of the initial ACCESS numerical weather prediction system. *Aust. Meteorol. Oceanogr. J.*, **63**, 265-284

Rosenfeld, D. et al. 2008: Flood or drought: How do aerosols affect precipitation? *Science* **321**(5894):1309–1313

Shige, S., Y.N. Takayabu, S. Kida, W.-K. Tao, X. Zeng, C. Yokoyama and T. L'Ecuyer, 2009: Spectral retrieval of latent heating profiles from TRMM PR data. Part IV: Comparison of lookup tables from two- and there-dimensional cloud-resolving model simulations. *J. Clim.*, **22**, 5577-5594

Smagorinsky, J., 1963: General circulation experiments with the primitive equations. I: The basic experiment. *Mon. Weather Rev.*, **91**, 99 – 164

Smith, RN.B., 1990: A scheme for predicting layer clouds and their water contents in a general circulation model. *Q. J. R. Meteorol. Soc.*, **116**, 435 – 460

Stith, J.L., J.E. Dye, A. Bansemer and A.J. Heymsfield, 2002: Microphysical observations of tropical clouds. *J. App. Meteor.*, **41**, 97 – 117

Stith, J.L., A. Hagerty, A.J. Heymsfield and C.A. Grainger, 2004: Microphysical characteristics of tropical updrafts in clean conditions. *J. App. Meteor.*, **43**, 779 – 794

Strapp, J. W., G. A. Isaac. A. Korolev, T. Ratvasky, R. Potts, P. May, A. Protat, P. Minnis, A. Ackerman, A. Fridlind, J. Haggerty, and J. Riley, 2015: The High Ice Water Content (HIWC) Study of deep convective clouds: Science and technical plan. FAA Rep. DOT/FAA/TC-14/31, in press

Tao, W.-K., J.R. Scala, B. Ferrier and J. Simpson, 1995: The effect of melting processes on the development of a tropical and midlatitude squall line. *J. Atmos. Sci.*, **52**, 1934 – 1948

VanWeverberg, K., A.M. Vogelmann, W. Lin, E.P. Luke, A. Cialella, P. Minnis, M. Khaiyer, E.R. Boer and M.P. Jensen, 2013: The role of cloud microphysics parameterisation in the simulation of mesoscale convective system clouds and precipitation in the Tropical Western Pacific. *J. Atmos. Sci.*, **70**, 1104 – 1181

Varble, A., A.M. Fridlind, E.J. Zipser, A.S. Ackerman, J.-P. Chaboureau, J. Fan, A. Hill, S.A. McFarlane, J.-P. Pinty and B. Shipway, 2011: Evaluation of cloud-resolving model intercomparison simulations using TWP-ICE observations: Precipitation and cloud structure. *J. Geophys. Res. Atmos.*, **116,** doi:10.1029/2010JD015180

Varble, A., E.J. Zipser, A.M. Fridlind, P. Zhu, A.S. Ackerman, J.-P. Chaboureau, S. Collis, J. Fan, A. Hill and B. Shipway, 2014: Evaluation of cloud-resolving and limited area model

intercomparison simulations using TWP-ICE observations. Part I: Deep convective updraft properties. *J. Geophys. Res. Atmos.*, **119,** 13891 – 13918

Varble, A., E.J. Zipser, A.M. Fridlind, P. Zhu, A.S. Ackerman, J.-P. Chaboureau, J. Fan, A. Hill, B. Shipway and C. Williams, 2014: Evaluation of cloud-resolving and limited area model intercomparison simulations using TWP-ICE observations. Part 2: Precipitation microphysics. *J. Geophys. Res. Atmos.*, **119,** doi:10.1002/2013JD021372

Waliser, D.E. et al., 2009: Cloud ice: A climate model challenge with signs and expectations of progress. *J. Geophys. Res.*, **114**, D00A21, doi:10.1029/2008JD010015

Walters, D. N., Brooks, M. E., Boutle, I. A., Melvin, T. R. O., Stratton, R. A., Bushell, A. C., Copsey, D., Earnshaw, P. E., Gross, M. S., Hardiman, S. C., Harris, C. M., Heming, J. T., Klingaman, N. P., Levine, R. C., Manners, J., Martin, G. M., Milton, S. F., Mittermaier, M. P., Morcrette, C. J., Riddick, T. C., Roberts, M. J., Selwood, P. M., Tennant,W.J., Vidale, P.-L.,Wilkinson, J. M., Wood, N., Woolnough, S. J., and Xavier, P. K.: The Met Office Unified Model Global Atmosphere 6.0 and JULES Global Land 6.0 configurations, in preparation, 2015.

Weusthoff, T., F. Ament, M. Arpagaus and M.W. Rotach, 2010: Assessing the benefits of convection-permitting models by neighbourhood verification: Examples from MAP D-PHASE. *Mon. Wea. Rev.*, **138**, 3418–3433

Wilkinson, J.M., 2013: *The Large-Scale Precipitation Parameterisation Scheme,* Unified Model Documentation Paper 26, Met Office, Exeter, UK. http://collab.metoffice.gov.uk/twiki/pub/Support/Umdp/026_84.pdf

Wilson, D.R. and S.P. Ballard, 1999: A microphysically based precipitation scheme for the UK Meteorological Office Unified Model. *Q. J. R. Meteorol. Soc.*, **125**, 1607 – 1636

Wilson, D.R., A.C. Bushell, A.M. Kerr-Munslow, D.P. Jeremy and C.J. Morcrette, 2008: PC2: A prognostic cloud fraction and condensation scheme. I: Scheme description. *Q. J. R. Meteorol. Soc.*, **134**, 2093 – 2107

Wisner, C., H.D. Orville and C. Myers, 1972: A numerical model of a hail bearing cloud. *J. Atmos. Sci.*, **29**, 1160 – 1181

Wood, N., Staniforth, A., White, A., Allen, T., Diamantakis, M., Gross, M., Melvin, T., Smith, C., Vosper, S., Zerroukat, M. and Thuburn, J., 2014: An inherently mass-conserving

semi-implicit semi-Lagrangian discretization of the deep-atmosphere global non-hydrostatic equations. Q.J.R. Meteorol. Soc., 140: 1505–1520. doi:10.1002/qj.2235

Yuter, S.E. and R.A. Houze Jr., 1995: Three-dimensional kinematic and microphysical evolution of Florida cumulonimbus. Part III: Vertical mass transport, mass divergence, and synthesis. *Mon. Wea. Rev.*, **123**, 1964 – 1983

Zipser, E.J., D.J. Cecil, C. Liu, S.W. Nesbitt and D.P. Yorty, 2006: Where are the most intense thunderstorms on Earth? *Bull. Amer. Meteor. Soc.*, **87**, 1057 - 1071

Atmos. Chem. Phys. Discuss., doi:10.5194/acp-2015-970, 2016
Manuscript under review for journal Atmos. Chem. Phys.
Published: 19 January 2016

Atmospheric Chemistry and Physics Discussions

Table 1. Parameters used to define the mass-diameter relationships (1) and particle size distributions (2), where $f(T)$ is given by (3).

Parameter	Units	Rain	Aggregates	Crystals	Graupel
a	kg m^{-b}	523.56	2.3 x 10^{-2}	2.3 x 10^{-2}	261.8
b		3.0	2.0	2.0	3.0
N_0	m^{-4}	$0.22\lambda^{2.2}$	2 x 10^6 $f(T)$	40 x 10^6 $f(T)$	5 x $10^{25}\lambda^{-4}$
μ		0	0	0	2.5

Atmos. Chem. Phys. Discuss., doi:10.5194/acp-2015-970, 2016
Manuscript under review for journal Atmos. Chem. Phys.
Published: 19 January 2016

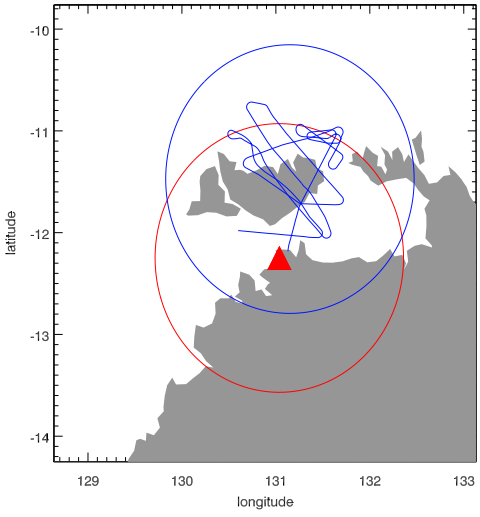

Figure 1. 1 km simulation domain with the radar location denoted by the red triangle and the 150 km range of the radar shown by the red circle. The aircraft flight track is shown by the blue line with the domain used in the aircraft comparison given by the blue circle.

Atmos. Chem. Phys. Discuss., doi:10.5194/acp-2015-970, 2016
Manuscript under review for journal Atmos. Chem. Phys.
Published: 19 January 2016

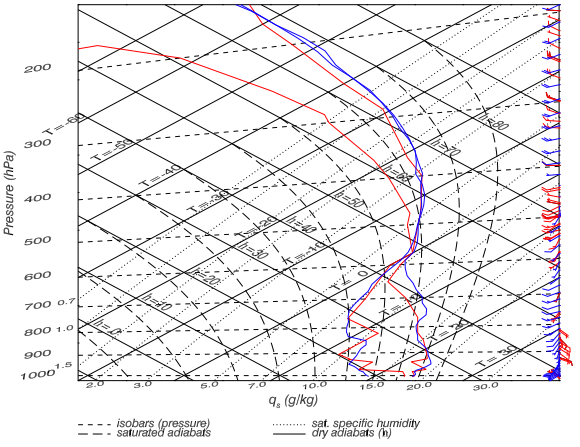

Figure 2. Thermodynamic diagram showing the observed (red) and modelled (blue) temperature, dew point temperature and winds for Darwin at 23 UTC 18/02/2014. A short/long wind barb represents 5/10 knots.

Atmos. Chem. Phys. Discuss., doi:10.5194/acp-2015-970, 2016
Manuscript under review for journal Atmos. Chem. Phys.
Published: 19 January 2016

Atmospheric Chemistry and Physics Discussions

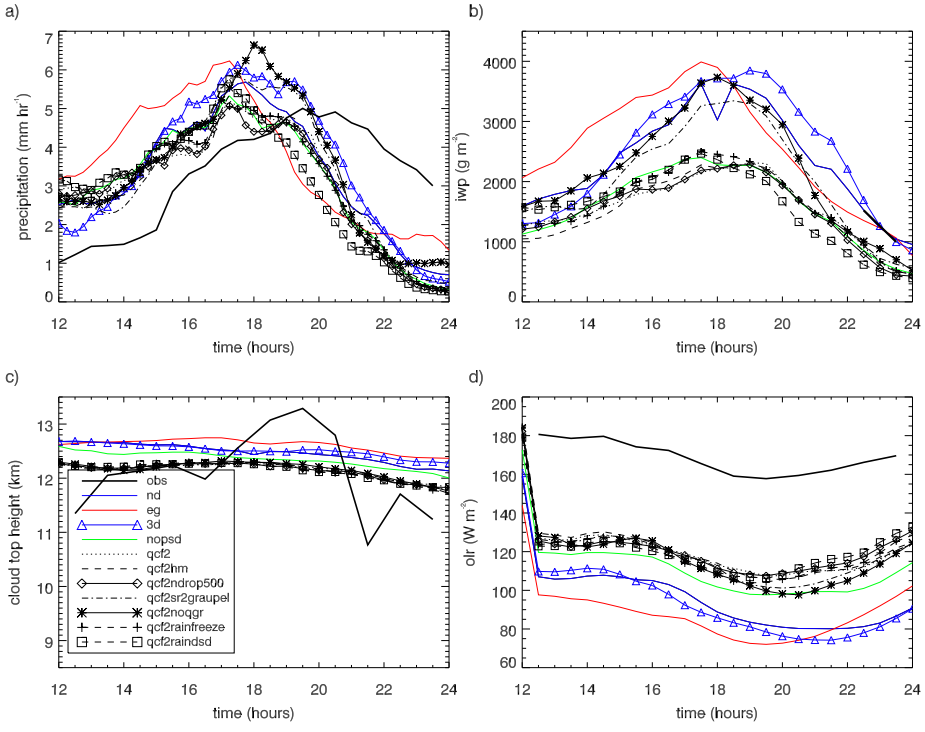

Figure 3. Time series of domain mean a) precipitation (mm hr^{-1}), b) ice water path (g m^{-3}), c) cloud top height (km) and d) outgoing longwave radiation (W m^{-2}). The observations are from the CPOL radar in a) and the satellite retrievals in the other panels (note that the observed IWP is only plotted from 22:30 – 23:30). The time period spans 12 – 24 UTC on 18/02/2014.

Atmos. Chem. Phys. Discuss., doi:10.5194/acp-2015-970, 2016
Manuscript under review for journal Atmos. Chem. Phys.
Published: 19 January 2016

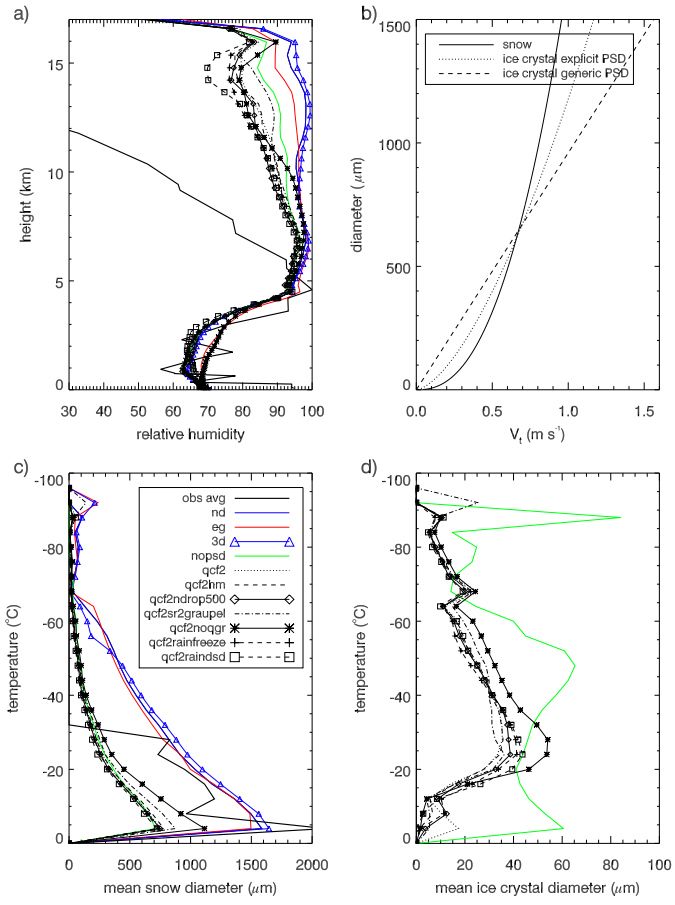

Figure 4. a) Observed relative humidity at Darwin on 18/02/2014 at 23 UTC in solid black line. Simulated relative humidity is for the area encompassed by the 150 km radius centred on the Darwin radar from 23 – 24 UTC. b) Ice fall speeds (m s^{-1}) as a function of diameter (μm) for the snow category and the ice crystals used in the simulations with the explicit and generic PSD, see text for details. c) Mean snow diameter (μm) as a function of temperature (ºC) where the observations are from the aircraft and have been averaged to be representative of a 1 km^2 grid cell. d) As for c) except for the mean ice crystal diameter (μm).

Atmos. Chem. Phys. Discuss., doi:10.5194/acp-2015-970, 2016
Manuscript under review for journal Atmos. Chem. Phys.
Published: 19 January 2016

Atmospheric Chemistry and Physics Discussions

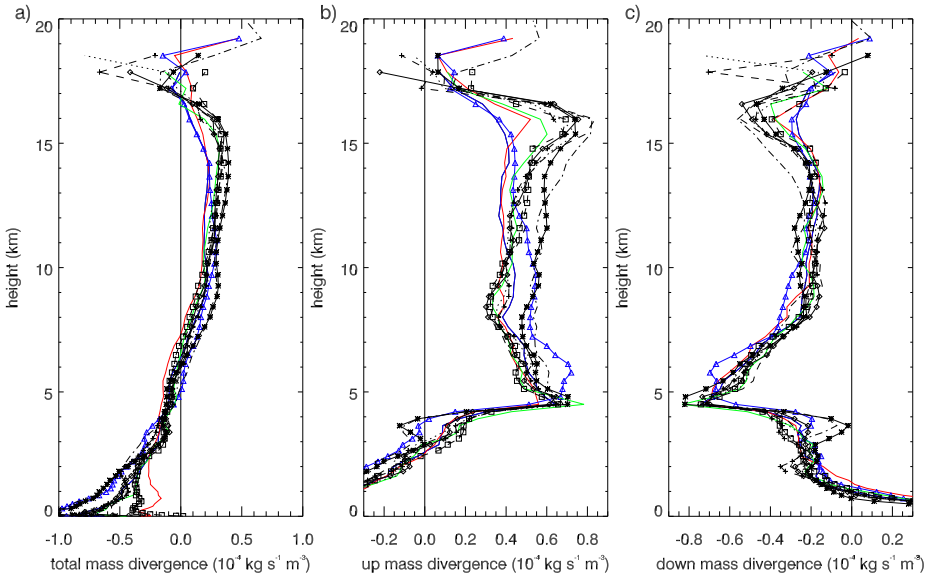

Figure 5. a) Vertical profile of mean horizontal mass divergence (10^{-4} kg s^{-1} m^{-3}) at 18 UTC, b) mean for the upwards vertical velocity, and c) for the downwards vertical velocity. The legend for the simulations is as in Figure 3.

Atmos. Chem. Phys. Discuss., doi:10.5194/acp-2015-970, 2016
Manuscript under review for journal Atmos. Chem. Phys.
Published: 19 January 2016

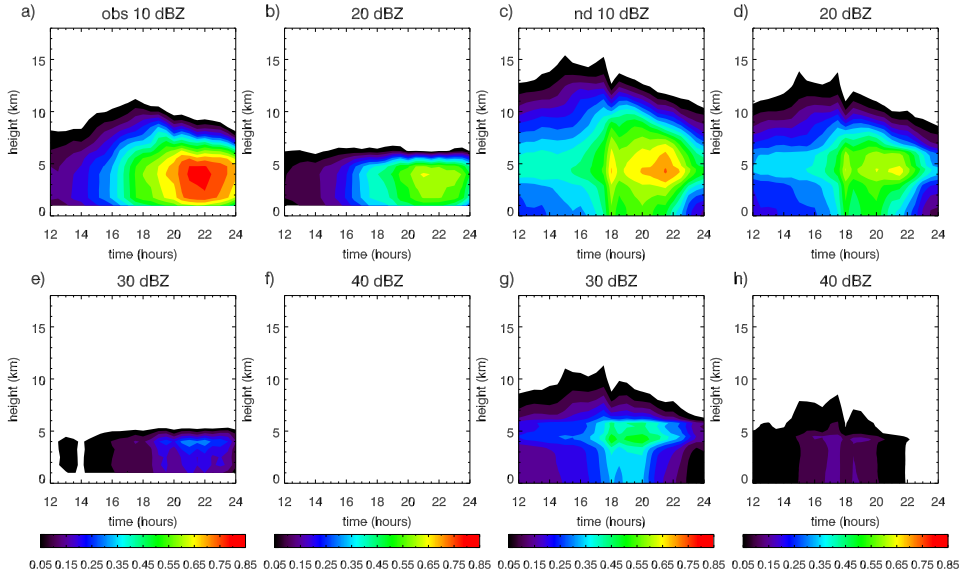

Figure 6. The observed (left 4 panels) and simulated (right 4 panels) fraction of radar detected area covered by reflectivities greater than a,c) 10, b,d) 20, e,g) 30 and f,h) 40 dBZ for 12 – 24 UTC on 18/02/2014.

Atmos. Chem. Phys. Discuss., doi:10.5194/acp-2015-970, 2016
Manuscript under review for journal Atmos. Chem. Phys.
Published: 19 January 2016

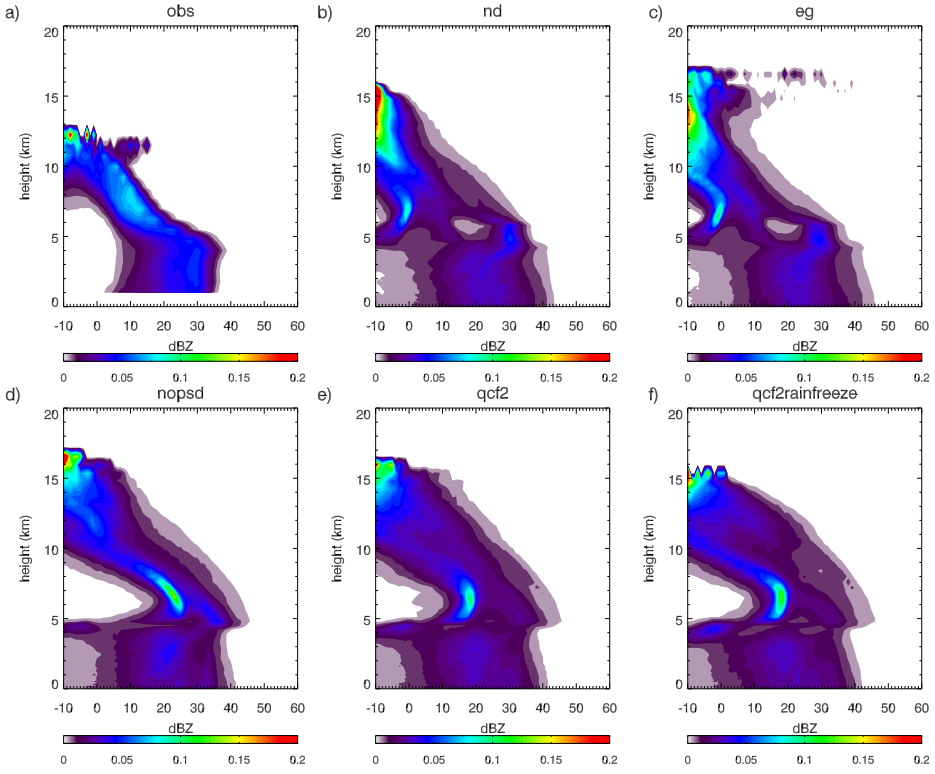

Figure 7. Contoured frequency with altitude diagrams of radar reflectivity for the region within 150 km of the radar for the times 23 – 24 UTC. a) Observations, b) control simulation, c) ENDGame dynamical core simulation, c) no use of the generic ice PSD parameterisation, d) additional ice prognostic and e) inclusion of heteorogeneous ice freezing parameterisation. See text for details on different simulations.

Atmos. Chem. Phys. Discuss., doi:10.5194/acp-2015-970, 2016
Manuscript under review for journal Atmos. Chem. Phys.
Published: 19 January 2016

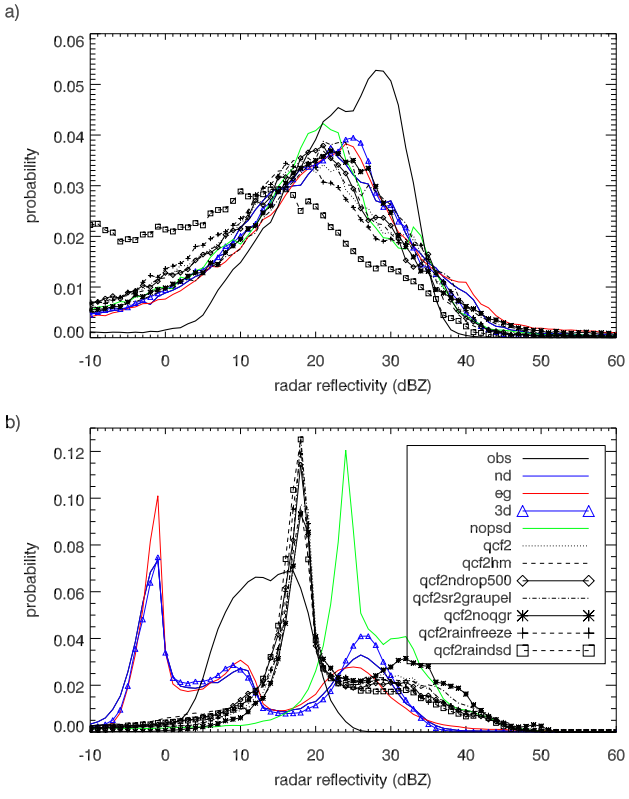

Figure 8. Radar reflectivity probability density functions for two heights, a) 2.5 and b) 6 km.

Atmos. Chem. Phys. Discuss., doi:10.5194/acp-2015-970, 2016
Manuscript under review for journal Atmos. Chem. Phys.
Published: 19 January 2016

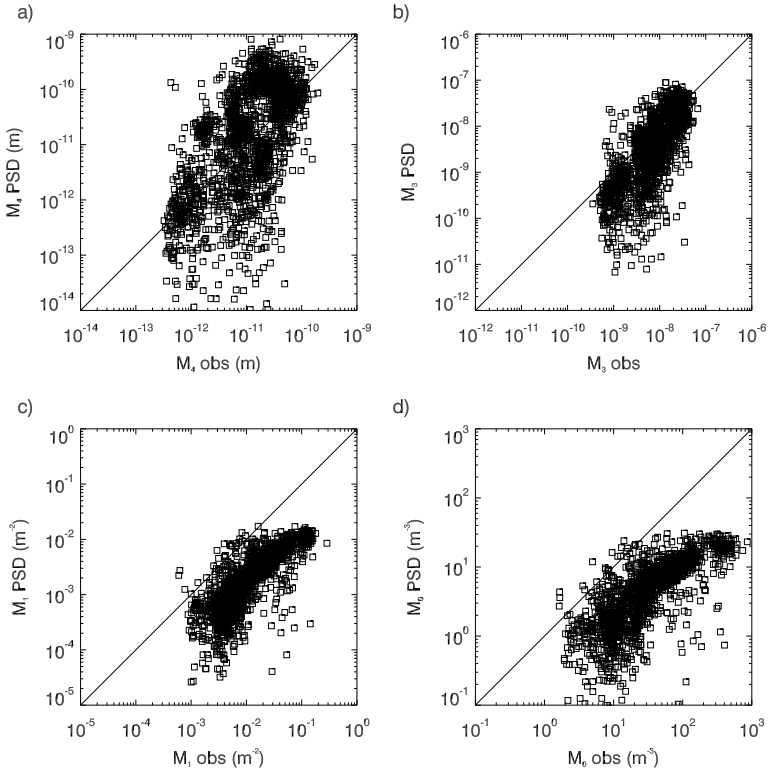

Figure 9. Moments (4th, 3rd; 1st and 0th) of the observed particle size distribution by the aircraft (for particles with diameters > 100 µm) and predicted using the PSD parameterisation with the observed ice water content (> 10^{-3} g m^{-3}), temperature and mass-diameter relationship.

Atmos. Chem. Phys. Discuss., doi:10.5194/acp-2015-970, 2016
Manuscript under review for journal Atmos. Chem. Phys.
Published: 19 January 2016

Atmospheric Chemistry and Physics Discussions

1

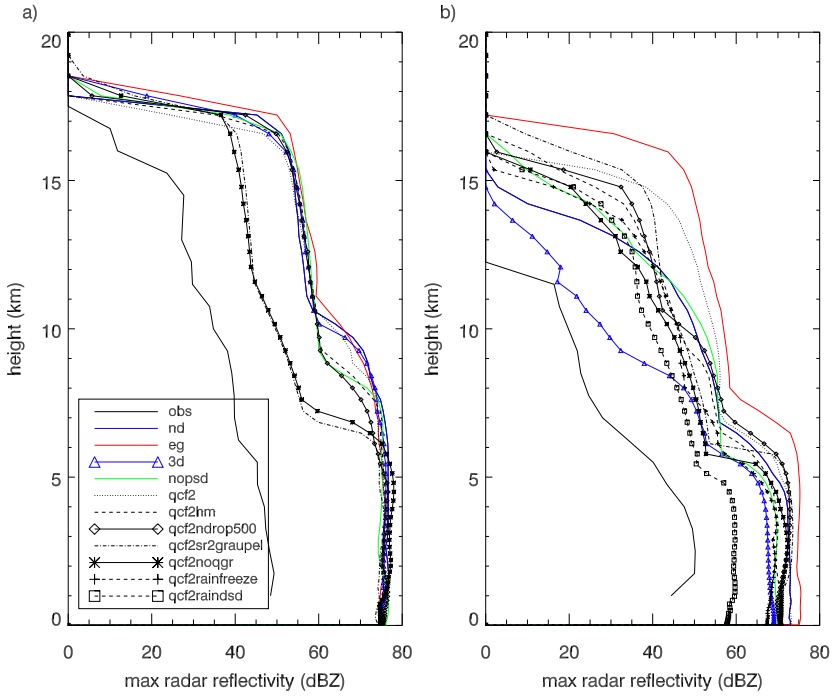

2

3 Figure 10. Profiles of maximum radar reflectivity for the times a) 17 – 18 UTC and b) 23 – 24

4 UTC.

5

Atmos. Chem. Phys. Discuss., doi:10.5194/acp-2015-970, 2016
Manuscript under review for journal Atmos. Chem. Phys.
Published: 19 January 2016

Atmospheric Chemistry and Physics Discussions

1

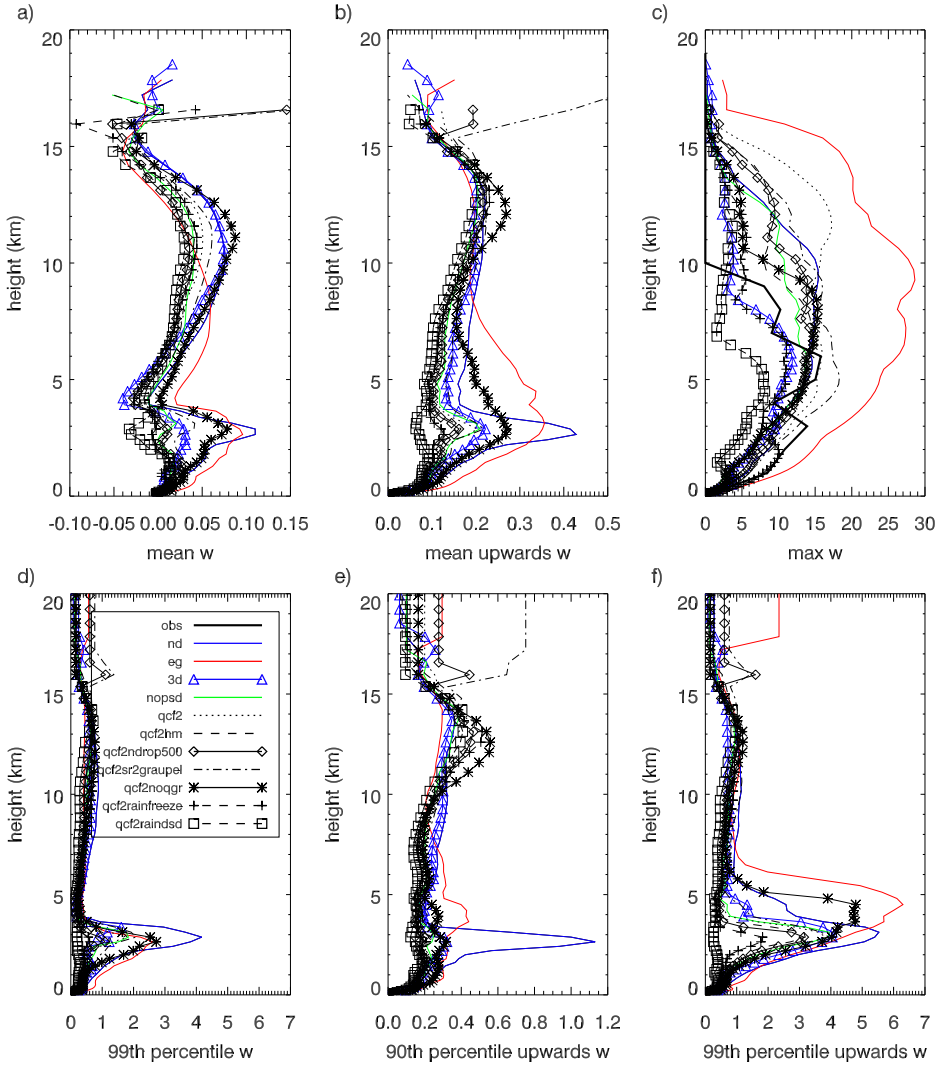

2

3 Figure 11. In-cloud vertical velocity statistics (m s^{-1}) over the radar domain for the times 23 –
4 24 UTC. a) Mean, b) updraft mean, c) maximum, d) 99th percentile, e) updraft 90th percentile
5 and f) updraft 99th percentile.

6

Atmos. Chem. Phys. Discuss., doi:10.5194/acp-2015-970, 2016
Manuscript under review for journal Atmos. Chem. Phys.
Published: 19 January 2016

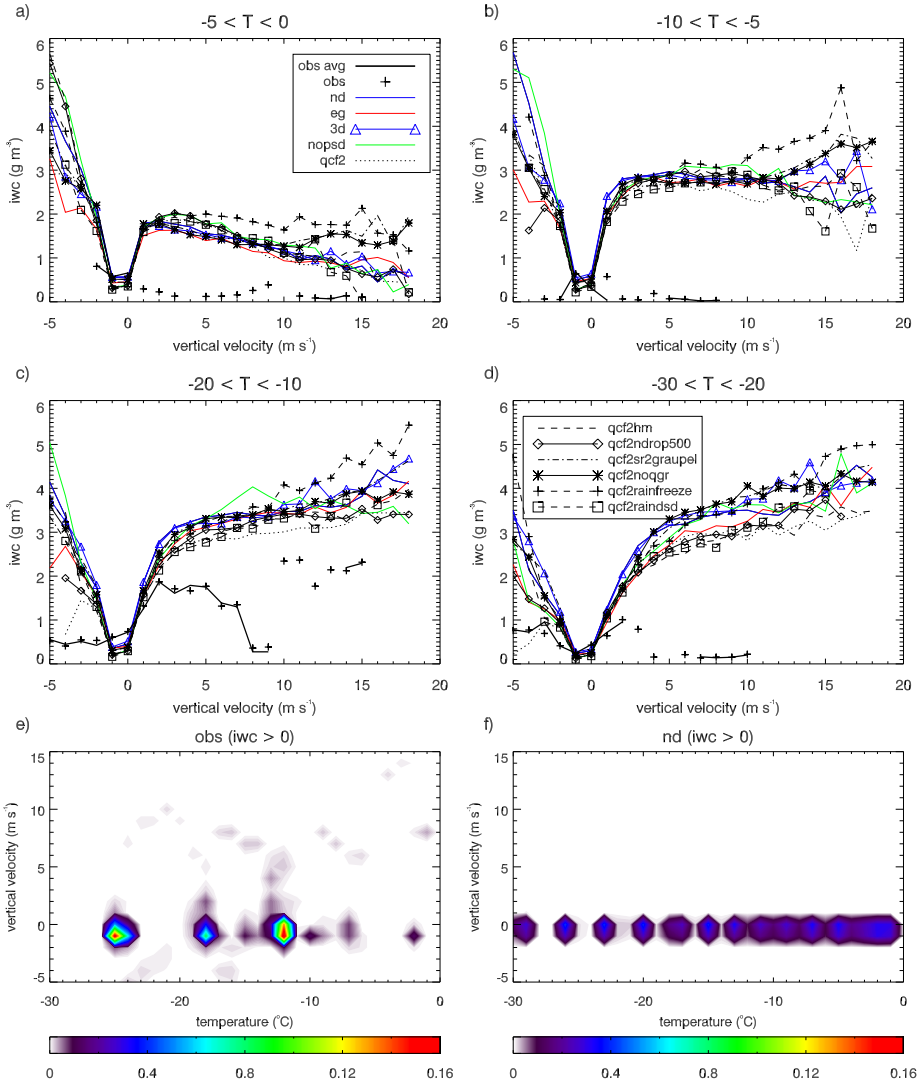

Figure 12. Ice water content (g m^{-3}) as a function of vertical velocity (m s^{-1}) for four temperature regimes: a) -5 – 0; b) -10 – -5; c) -20 – -10, and; d) -30 – -20 ºC. e) and f) show the joint probability density functions of vertical velocity and temperature for the observations and the control 1 km simulation for regions with IWC > 0.

Atmos. Chem. Phys. Discuss., doi:10.5194/acp-2015-970, 2016
Manuscript under review for journal Atmos. Chem. Phys.
Published: 19 January 2016

1

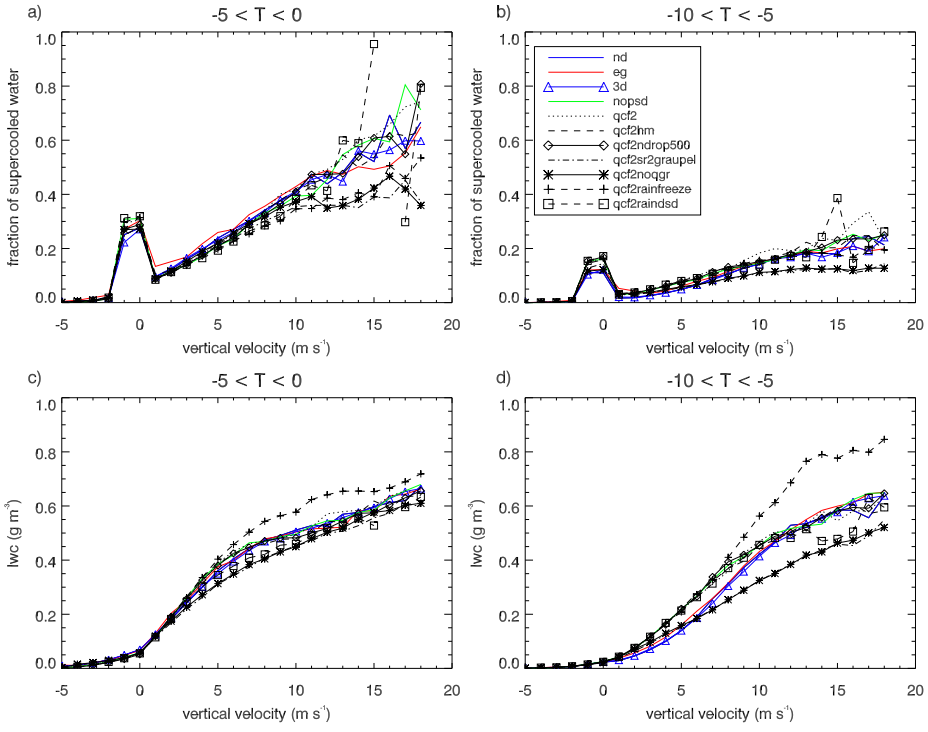

2

3 Figure 13. a), b) Fraction of condensate that is supercooled cloud liquid water, c), d) liquid
4 water content (g m^{-3}) for the two warmer temperature regimes a), c) -5 – 0 and b), d) -10 – -5
5 ºC.
6

Atmos. Chem. Phys. Discuss., doi:10.5194/acp-2015-970, 2016
Manuscript under review for journal Atmos. Chem. Phys.
Published: 19 January 2016

Atmospheric Chemistry and Physics Discussions

1

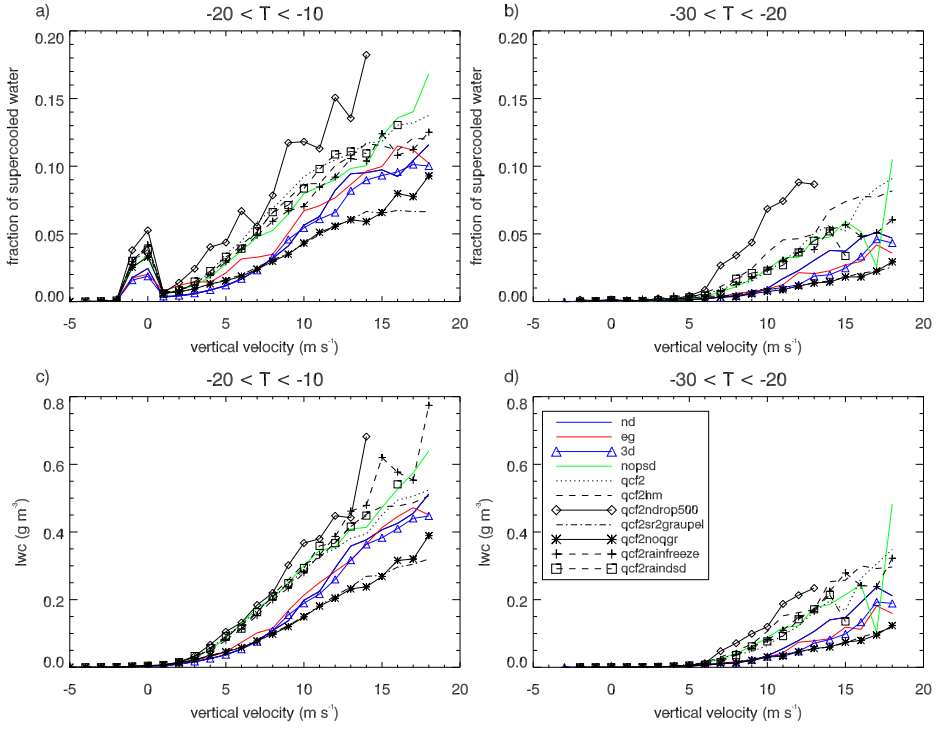

2

3 Figure 14. As in Figure 9 except for the two colder temperature regimes: a), c) -20 – -10 and
4 b), d) -30 – -20 °C.

5

Atmos. Chem. Phys. Discuss., doi:10.5194/acp-2015-970, 2016
Manuscript under review for journal Atmos. Chem. Phys.
Published: 19 January 2016

Atmospheric Chemistry and Physics Discussions

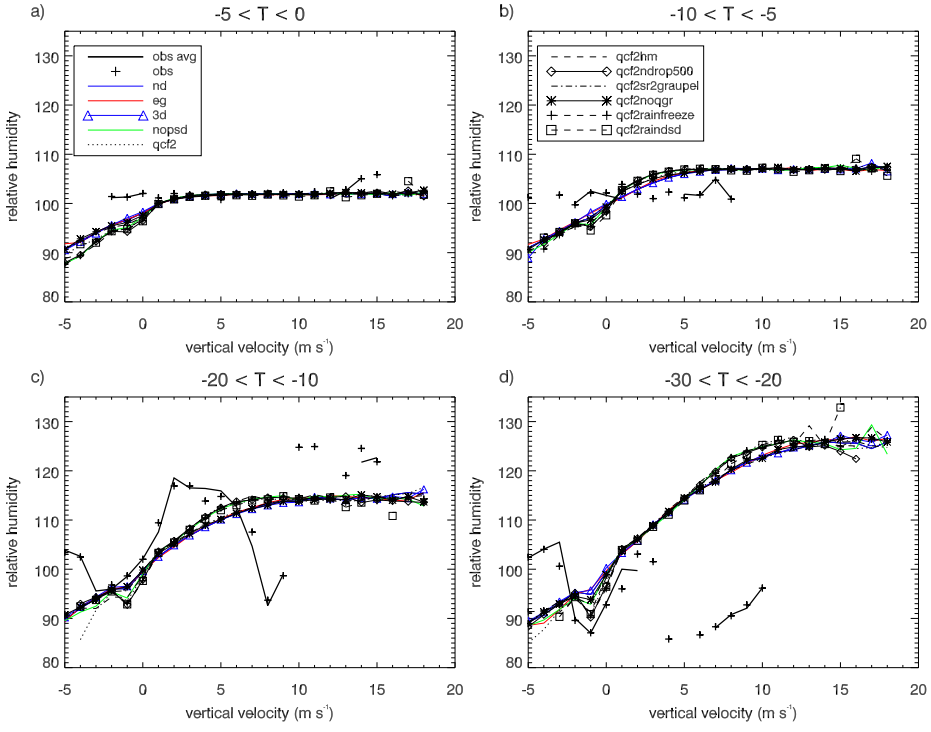

Figure 15. As in Figure 8 accept for relative humidity as a function of vertical velocity for the four temperature regimes.

Atmos. Chem. Phys. Discuss., doi:10.5194/acp-2015-970, 2016
Manuscript under review for journal Atmos. Chem. Phys.
Published: 19 January 2016

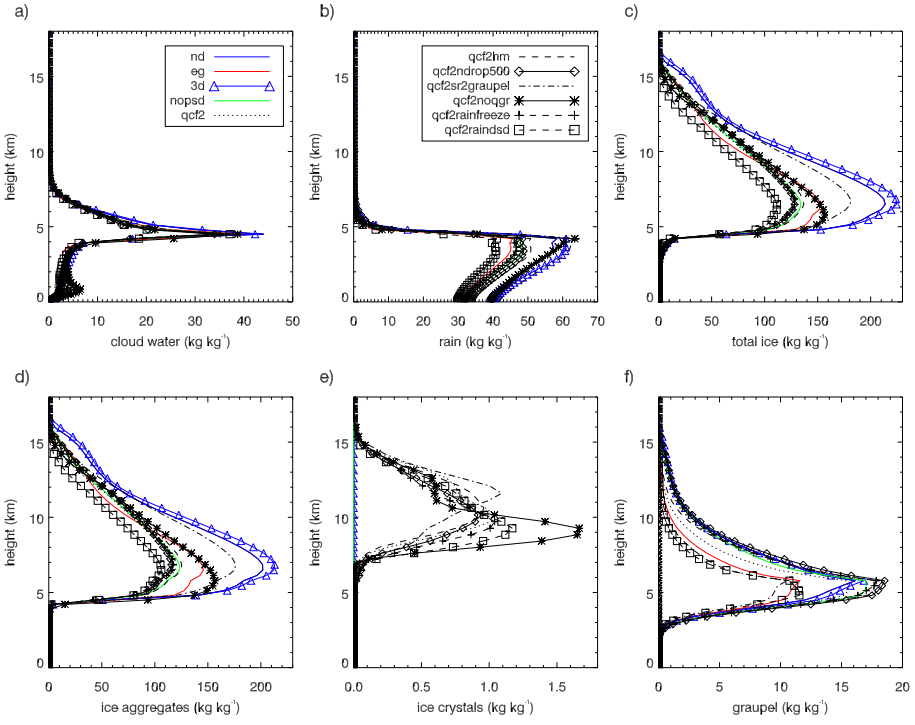

Figure 16. For the aircraft analysis region (150 km radius from the mean aircraft track), the total accumulated water contents (kg kg^{-1}) over the domain from 23 – 24 UTC. a) Cloud liquid water, b) rain water, c) total ice, d) ice aggregates/snow, e) ice crystals and f) graupel.

Atmos. Chem. Phys. Discuss., doi:10.5194/acp-2015-970, 2016
Manuscript under review for journal Atmos. Chem. Phys.
Published: 19 January 2016

Atmospheric Chemistry and Physics Discussions

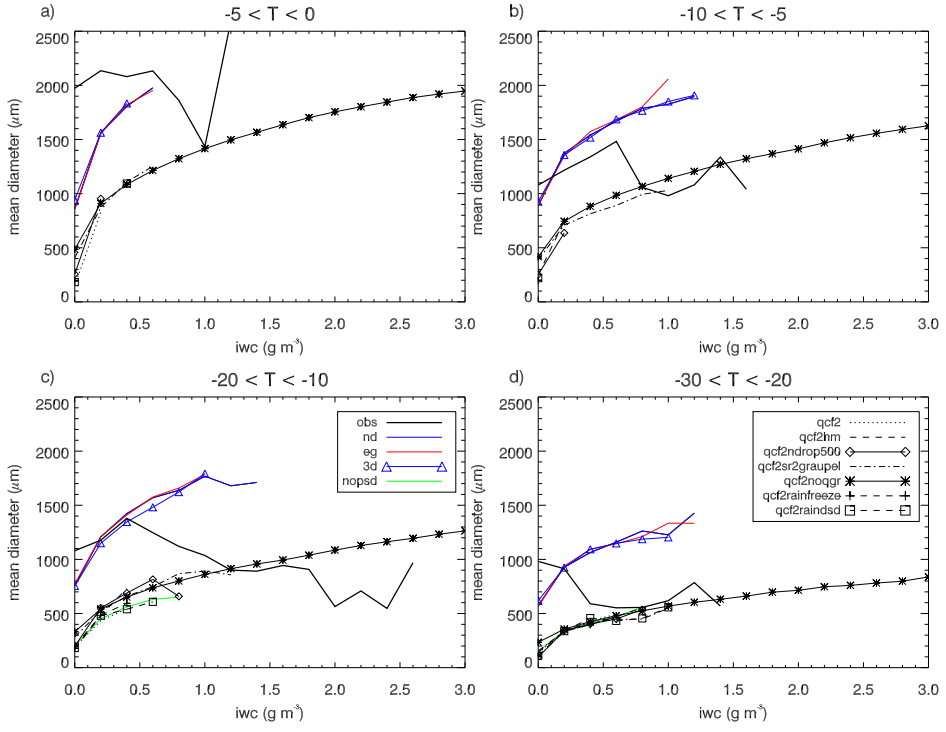

Figure 17. Mean mass-weighted ice particle size (μm) as a function of ice water content (g m^{-3}) for four temperature regimes: a) -5 – 0, b) -10 – -5, c) -20 – -10, and; d) -30 – -20 ºC.